ARMENIAN RENEWABLE RESOURCES AND ENERGY EFFICIENCY FUND

"GEORISK" SCIENTIFIC RESEARCH COMPANY

Independent interpretation of the results of the 3D MT, gravity and CO$_2$ surveys conducted at the Karkar Site

Project GEF-CS-4/2008

Preliminary report

georisk

R$_2$E^2

ARMENIAN RENEWABLE RESOURCES AND ENERGY EFFICIENCY FUND

"GEORISK" SCIENTIFIC RESEARCH COMPAN

Independent interpretation of the results of the 3D MT, gravity and CO2 surveys conducted at the Karkar Site

Project GEF-CS-4/2008

Preliminary report

April, 2012

Contents

List of Figures

0. Executive Summary

1. Introduction

This document presents a preliminary report on the review and interpretation of the geophysical analyses and report prepared by WesternGeco staff in 2011 for geothermal assessment of the Kar Kar area, Armenia. The purposes of this review are to assess the overall quality of the geothermal resource, to identify best drilling targets, and to make recommendations for next steps in the exploration program. To this end, our review consists of several parts:

1. Magnetotelluric (MT) data collected by WesternGeco are reviewed and compared with model results from previous surveys.

2. Gravity data collected by WesternGeco are reviewed and analyzed. A new gravity inversion is performed to estimate the depth of a fault-bounded basin in the Kar Kar region.

3. A new hydrothermal model is constructed based on bounding conditions that emerge from interpretation of the MT, gravity, and borehole data.

The geological interpretation, geothermal model and conceptual model, and recommendations will be included in the Final Project report.

1.1 Scope

Data discussed in this report were collected by WesternGeco staff in the late summer of 2011. Additional data collected jointly by the staff of GEORISK CJS (Armenia) and USF (USA) in the summer of 2009, and in 2004 by the Russian and Armenian Academies of Sciences, are included and discussed where appropriate. These additional data include information gathered from borehole4 in the Kar Kar region, and 2D MT surveys conducted by GEORISK/USF staff in 2009.

This report is primarily a review of the WesternGeco data and models. In addition, new gravity inversion results are presented and a new hydrothermal model is developed in order to assist in the interpretation of geophysical data. Recommendations are made regarding the next steps in exploration of potential geothermal resources in the Kar Kar region, in light of these data, models, and interpretation.

2. Analysis of MT portions of the WesternGeco report (2011)

Magnetotelluric (MT) soundings provide critical information for the evaluation of geothermal resources. In the following, we show that broadly speaking, MT data collected in 2004, 2009, and 2011 in the Kar Kar area provide consistent results. Low resistivity anomalies are located in both 2D and 3D inversion models, most prominently at 2000-2500 masl and east of Borehole4 and the Jermaghbyur hot springs. These low resistivity anomalies extend as discrete zones into the fault-bounded graben to the east. Within this fault-bounded graben, low resistivity anomalies extend to slightly greater depths, on order 1500 masl.

In the following results of the 2011 MT survey by WesternGeco are reviewed and compared with results of earlier surveys.

2.1 Comparing locations of MT Data Collection from the 2004, 2009, and 2011 MT Surveys

WesternGeco MT data were collected in 2011. This is the third MT survey in the region that we are aware of, each conducted for the purpose of exploration of potential geothermal resources. MT and audiomagnetotelluric (AMT) data were acquired previously by the Institute of Geophysics and Engineering Seismology (IGES) of the National Academy of Sciences o Armenia, in cooperation with the Moscow State University. That survey took place in 2004, and their data acquisition was mostly west of the WesternGeco survey area, focusing at the Jermaghbyur hot springs site. A second survey was conducted in 2009 jointly by the GEORISK Scientific Research CJS (Armenia) and University of South Florida (USF). This survey included a traverse from the hot spring area east, through the area surveyed by WesternGeco, a region inferred to be a fault-bounded basin based on geological mapping and structural analysis by staff of the Armenian National Academy of Sciences. The WesternGeco MT survey, the most detailed to date, consisted of a grid of MT data acquisition across the fault-bounded basin.

The locations of the 2004 MT (and AMT) sites are shown in Figure 1. The 2009 GEORISK/ USF MT survey station locations (along with TEM soundings) are shown in Figure 2. In order to compare the 2004 and 2009 geophysical surveys, Figure 3 shows a map with the positions of sites from both surveys. As can be seen in Figure 3, the 2009 geophysical survey overlap the northern portion of the 2004 geophysical survey, and the 2009 data extended much further east.

The geophysical data acquisition positions from the 2011 WesternGeco report are shown co-located with the 2009 MT sites in Figure 4.

We note that Dr. Piotr Dlugosz, in his review dated January 4, 2012, emphasized the need to collect data west of the WesternGeco survey area, encompassing the Jermaghbyur hot springs site. We agree that correlation between the WesternGeco survey and the existing hot springs is important. We also add that the data acquired in 2009 by the GEORISK and University of South Florida (USF) does extend to the hot springs, as shown in Figure 2. We address the consistency and repeatability of the data from these two surveys in a following section of this report. Nevertheless, it is clear that utility of the 3D modeling performed by WesternGeco would have been greatly enhanced by jointly modeling the 2009 GEORISK/USF data with the data collected by WesternGeco in 2011.

2.2 Numerical Modeling Used in the MT Survey Interpretations

The 2004 MT survey was modeled and interpreted using 1D models of individual sites, stitched together to form 2D models. The GEORISK/USF 2009 data were modeled using 2D inverse modeling, and the 2011 WesternGeco data were modeled using a full 3D inversion modeling code. This 3D inversion modeling code is state-of the-art, and considered to be perhaps the best MT modeling code available. The WesternGeco 3D model should provide a more accurate view of the resistivity distribution in the subsurface than was possible using 1D and 2D inverse models. However, the MT data themselves, which are exemplary, indicate that in some parts of the field area 1D and/or 2D modeling may be sufficient. With regard to interpretation of the 2009 survey results, it was noted that in the data pseudosections the TM and TE modes have a lot of similarities, indicating that the profile is largely 1D, which was also indicated by the semi-layering of resistivity in the 2D model. Also, the 10 Hz polar diagrams for the 2009 data become quite circular, also indicating 1D tendency, at least in the shallow subsurface. Although not discussed in the 2009 report, the 10 second polar diagrams (Figure 18 of that report) indicate similarity of orientation for most sites, with the principal axis approximately in the west-northwest direction, supporting the N90E rotation prior to 2D modeling.
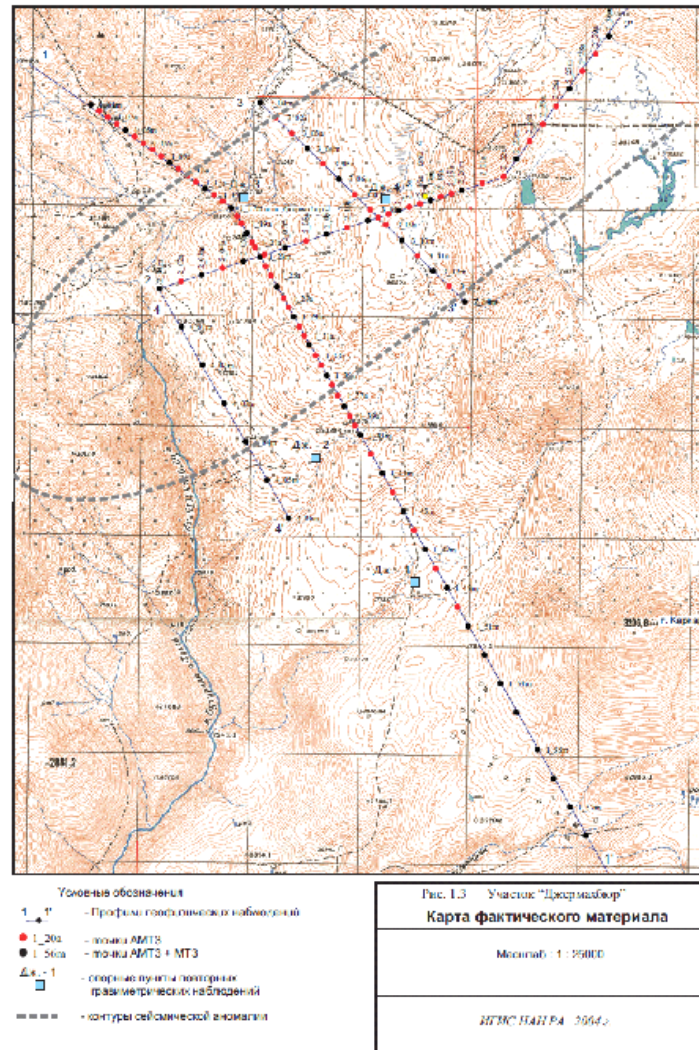
Figure 1: MT and AMT sites from the 2004 geophysical survey. Survey completed by the Institute of Geophysics and Engineering Seismology (IGES) of the NAS of the RA, in cooperation with the Moscow State University.
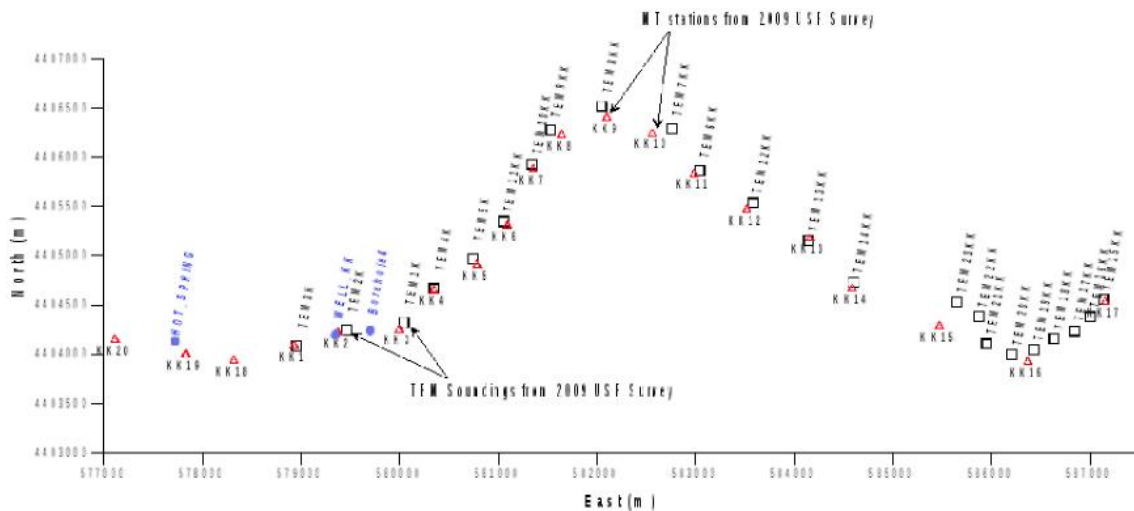
Figure 2: MT and TEM data acquisition sites from the GEORISK/ USF 2009 geophysical survey. Also shown are the locations of the Jermaghbyur hot spring site, and the location of Borehole4 (based upon the coordinates provided by the Armenian National Academy of Sciences and GeoRisk). Another well shown, WELL KK, was identified by the Armenian field crew during the 2009 survey, although the well was not actually seen by USF personnel. Further discussions indicate that it is likely that that well and Borehole 4 are the same feature.
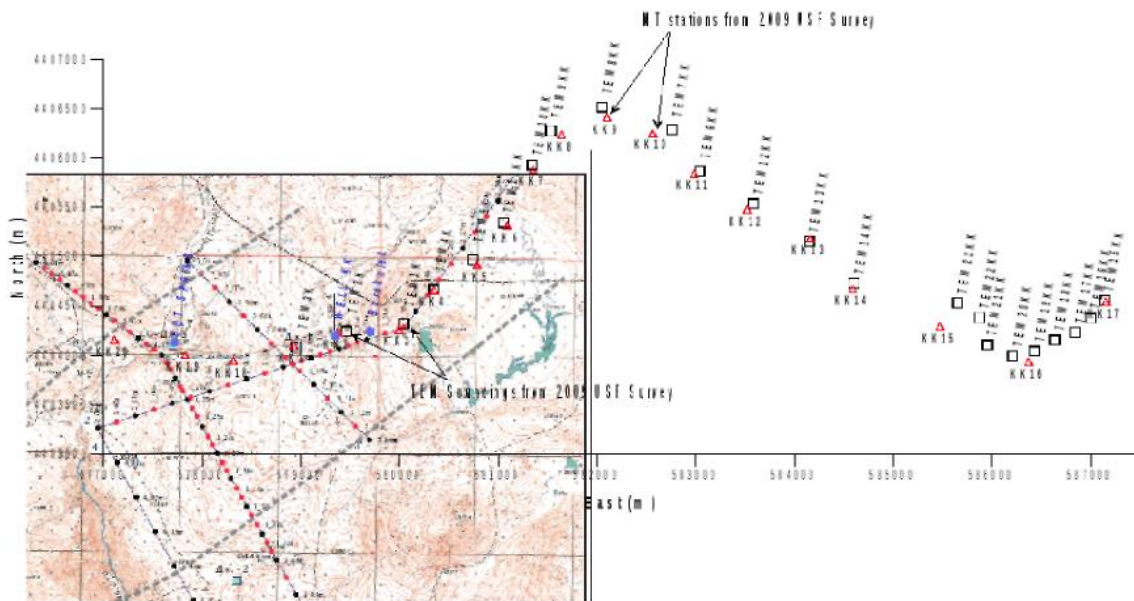
Figure 3: Locations of the 2004 and 2009 surveys, referenced together. This map was constructed by positioning a portion of Figure 1 on the Figure 2 map as best as possible. The actual coordinates of the 2004 data acquisition positions were not available for co-rendering.

8

USF 2009 MT Stations
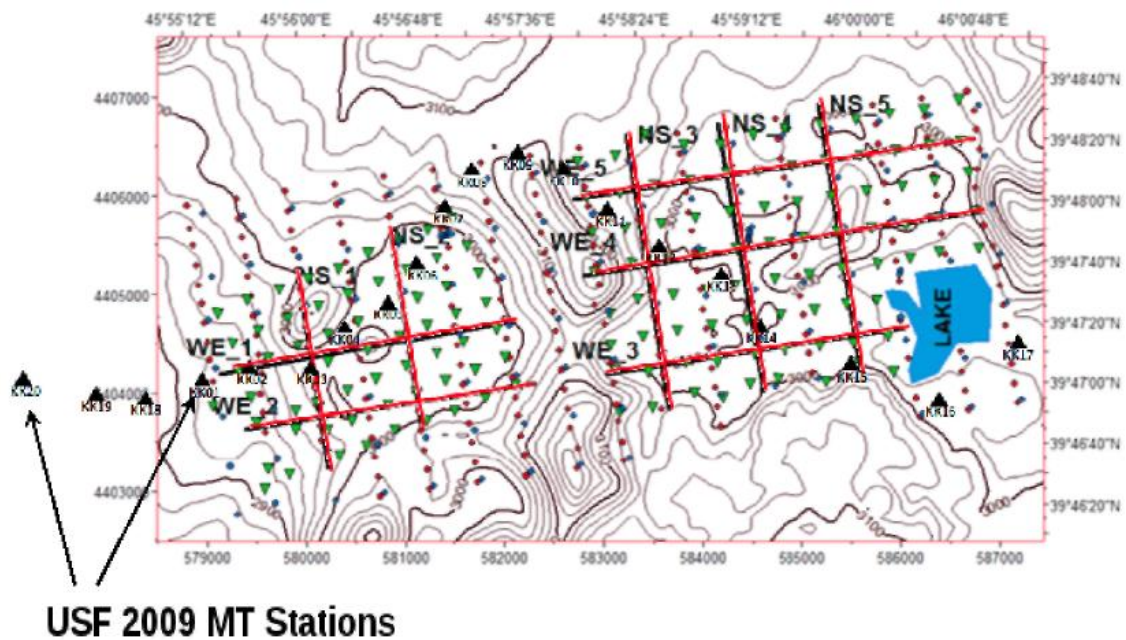
Figure 4: The GEORISK//USF 2009 MT stations co-located on the station location map
from the WesternGeco report (2011).

In addition, Figure 5 shows induction arrows calculated from the 2004 MT data. Note
the consistent directions of arrows in the northeastern portion of the map, where the 2009 MT
data were collected, and where some of the 2011 WesternGeco data were collected. This
indicator of dimensionality also suggests that a 2D modeling approach could be applied in that
area with good results. Therefore, MT results suggest that it is reasonable to compare 2D and 3D
inversion models based on 2009 and 2011 surveys, respectively, with the caveat that more
detailed and very high quality of data collection in 2011 should improve model resolution.

2.3 Comparison of 3D (WesternGeco,2011) and 2D (GEORISK/USF, 2009). Inverse Models

WesternGeco resistivity/depth from the 3D model are presented in two formats in their
report. First, a series of 10 cross-sections are presented, as indexed in Figure1 of their report,
and reproduced as part of Figure 4 above. Figure 6 shows these cross-sections in relation to the
2009 MT survey positions. Second, the WesternGeco 3D model is illustrated by depth slices,
showing resistivity in map view versus elevation for horizontal slices at 1000, 1500, 2000, 2250,
2500, 2750, and 3000 masl. We begin by comparing cross-sections for the 2D (USF, 2009) and
3D (WesternGeco, 2011) models.

The 2D GEORISK/USF 2009 model is compared with sections WE 1 and WE 3 of the
3D WesternGeco 2011 model. Only these two sections can be readily compared, due to the
geometry of the station positions and the orientation of the 2009 2D profile.
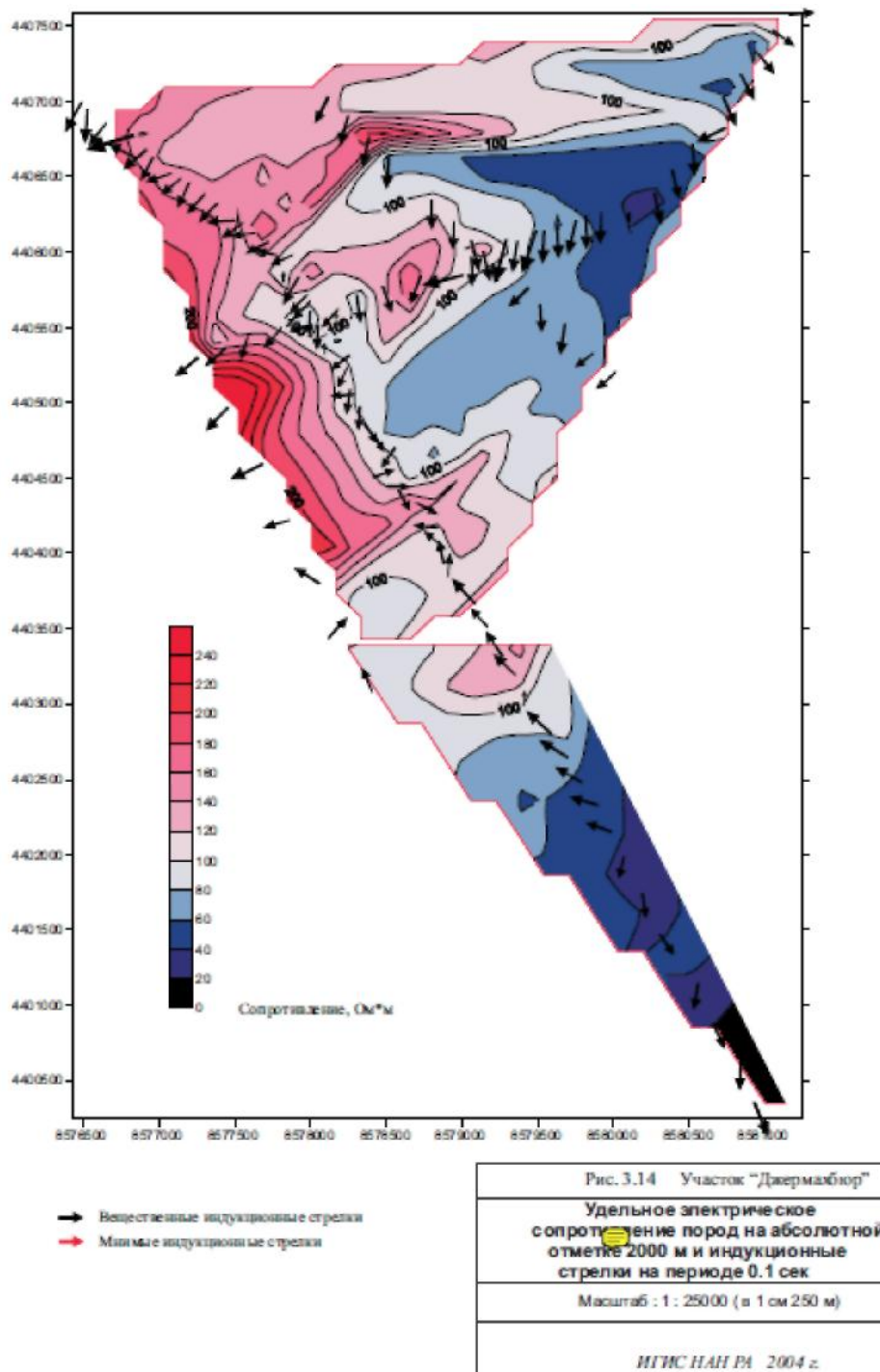
Figure 5: Induction arrows at 10 s period, superimposed on resistivity at 2000 m elevation from the 2004 geophysical survey.
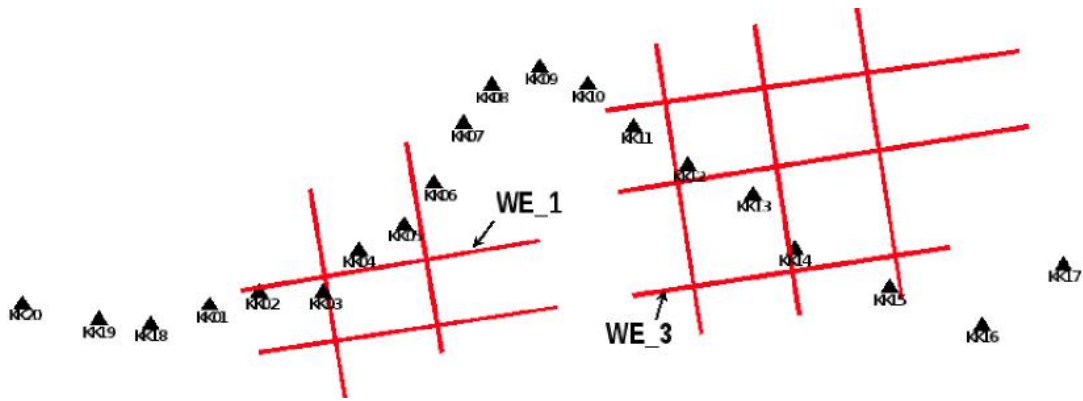
Figure 6: The 10 cross-sections of the WesternGeco 3D MT model presented in their report, superimposed on the MT sites from the 2009 survey. Cross-sections WE 1 and WE 3 are labeled.

2.3.1 Section WE 1

Figure 7 shows the western portion of 2D Model 3 from the 2009 GEORISK/ USF interpretation. Borehole 4 is also shown, as well as the position of a water bearing interval in that borehole, interpreted from the model. Note the spatial correlation of this water-bearing zone with the low-resistivity zone extending east of the well (the blue/purple region in the model). However, there is a gap between the borehole and that lowest resistivities at this stratigraphic level, of approximately 1500 m.

WesternGeco section WE 1 is shown in Figure 8, co-located over the western portion of the 2009 GEORISK/USF model from Figure 7. It is important to recognize that the resistivity color scales are opposite; low resistivity on the 2009 model is represented by blue and green, whereas low resistivity on the WesternGeco section is represented by red and yellow. Without obtaining the proprietary software used by WesternGeco to generate these figures, the resistivity anomalies could to be rendered on an equivalent color scale.

In order to compare these two resistivity distributions, Figure 9 shows a relatively shallow region of low-resistivity in the 3D model enclosed by a heavy dashed line. In addition, another heavy dashed line deeper in the section marks where the resistivity of the 3D model increases with depth. Figure 10 shows these two interpreted features (heavy dashed lines) transferred onto the 2009 2D model from Figure 7. It is evident by comparing Figure 9 and Figure 10 that the two features are present in both the 2D model and the 3D model. This suggests consistency in location and depth of resistivity anomalies between the two models.

We note there is a discrepancy between the 2D and 3D models involving the lower resistivity contact between stratigraphically higher low resistivity and stratigraphically deeper high resistivity units. This contact is shown by the heavy dashed line on Figures 9 and 10. In the 3D model, this resistivity contrast is depicted as a linear, east-dipping contact. On the 2D model, this feature is shown as a basement (?) resistivity high, reaching approximately 1500 masl at its shallowest point, but dipping west and east from this point along the profile. By comparison with borehole 4 stratigraphic logs, discussed in detail later in this report, it appears likely that this high resistivity zone correlates with unfractured igneous intrusion, lying beneath fractured igneous intrusion (quartz monzonite). The discrepancy between the 2D and 3D models in this area is caused by extrapolation of the 3D model toward the west, away from the data control of the 2011 survey grid. This results in a shallowing of that interface toward the west as depicted in the 3D model (Figure 9). However, the 2D model is based upon 2009 data that extends further west, namely to stations KK01, KK18, KK19, and KK20, thus avoiding the need to extrapolate the model. This result indicates it would have been preferable for WesternGeco to include the 2009 profile data in their 3D model.
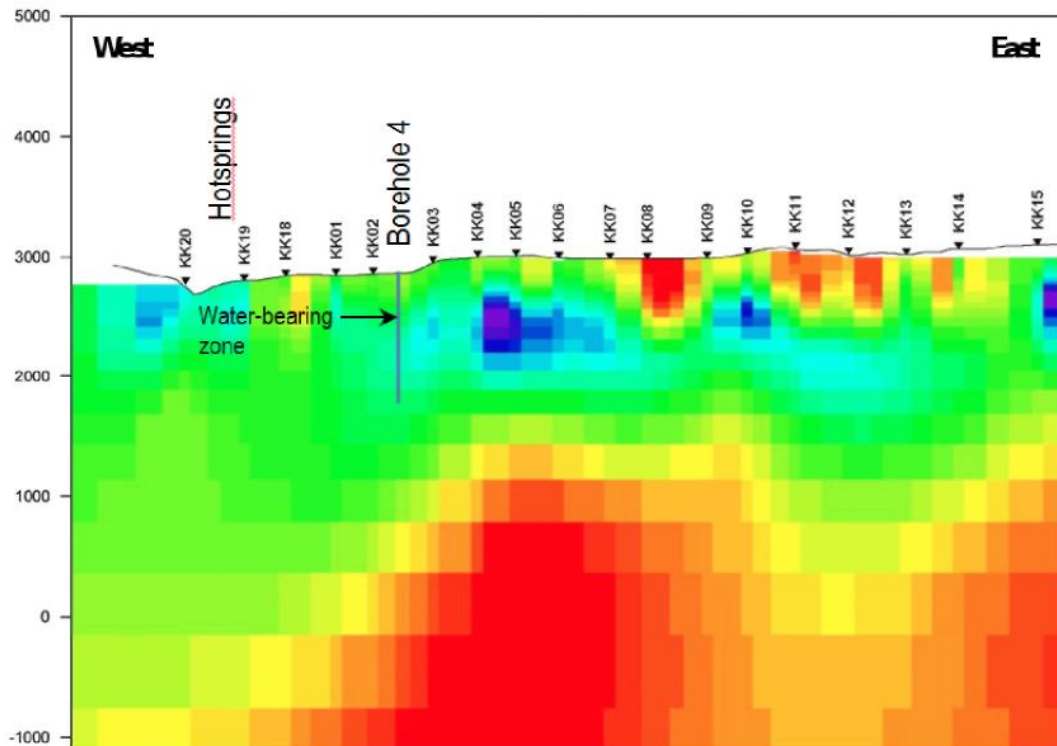
Figure 7: The western portion of the 2D model 3 (USF, 2009). Also shown in the figure are the locations of the hot springs, and Borehole 4. In addition, the location of an interpreted water-bearing zone encountered in the borehole is shown.
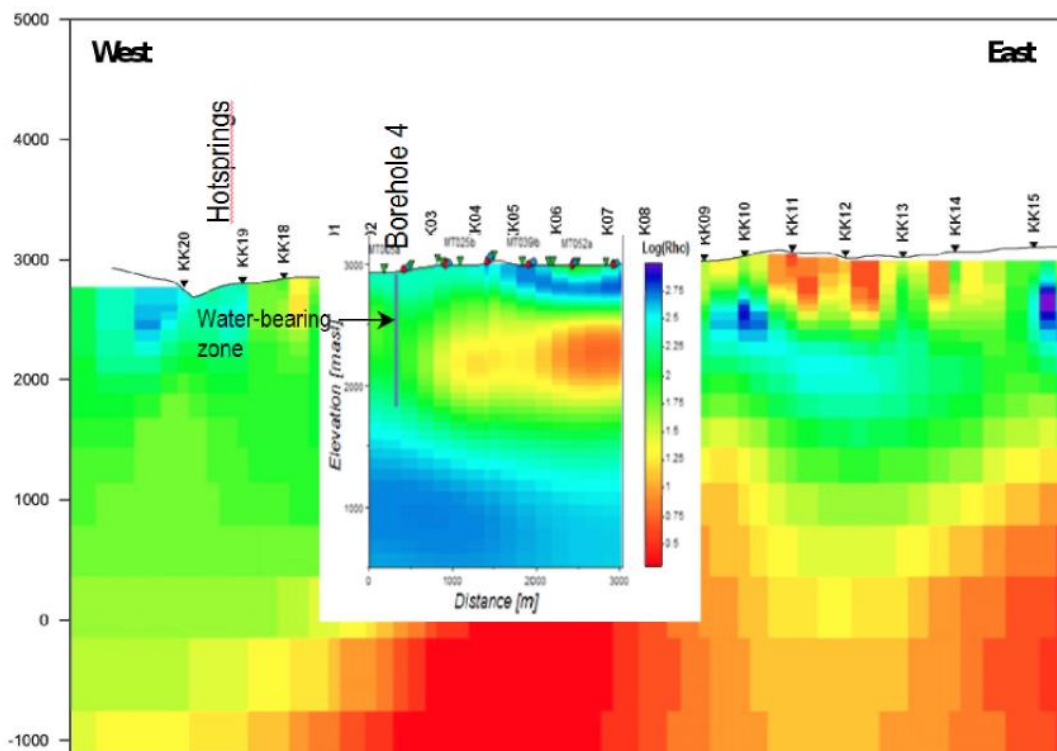
Figure 8: WesternGeco section WE 1 co-located on top of the 2009 GEORISK/USF model. Note that the resistivity color scales are opposite; low resistivity on the 2009 model is represented by blue and green, whereas low resistivity on the WesternGeco section is represented by red and yellow.
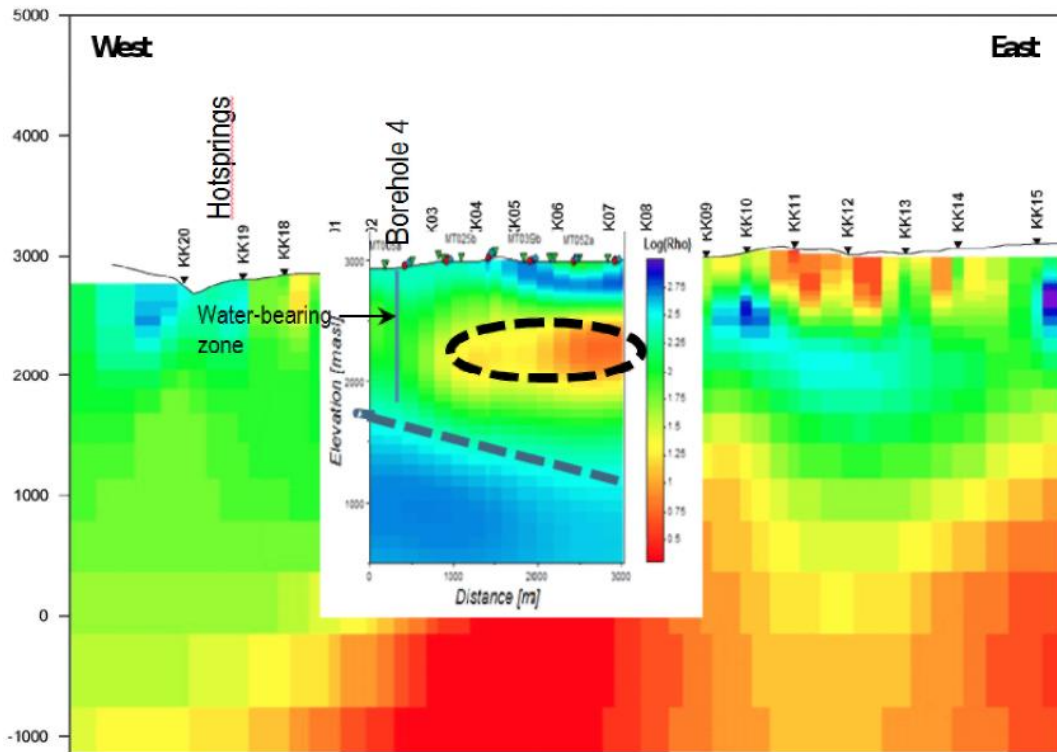
Figure 9: Resistivity section WE 1 co-located on top of the 2009 GEORISK/USF model, as in Figure 8, except interpreted features have been drawn with heavy dashed lines.
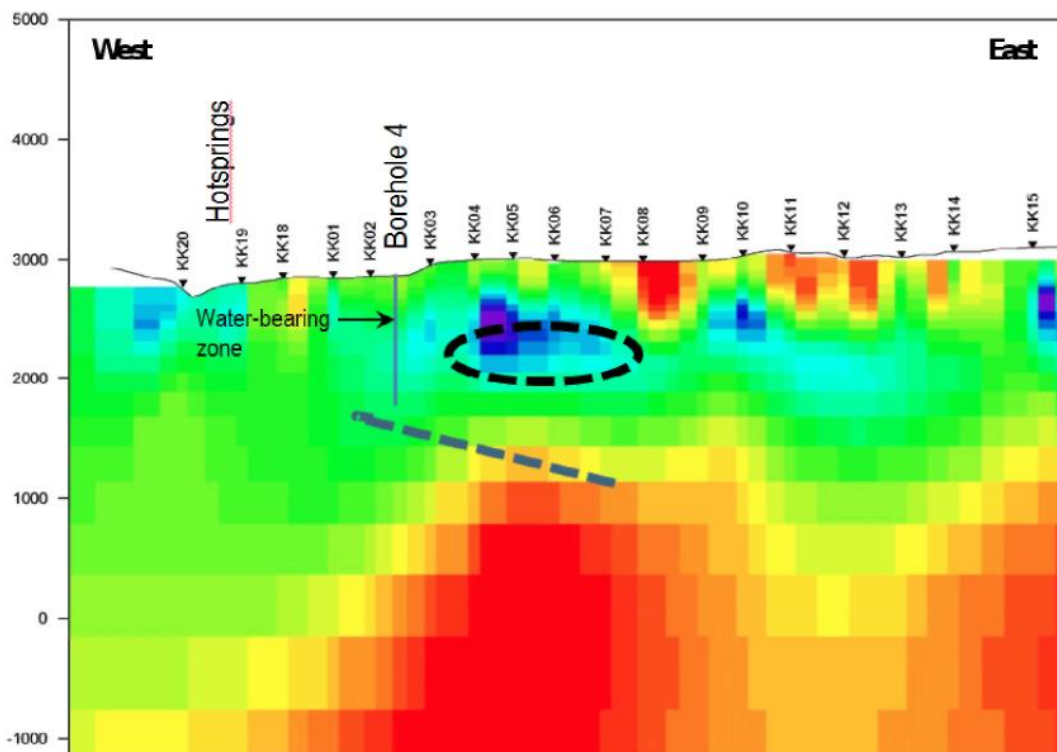
Figure 10: The 2D model (USF, 2009), as in Figure 7, except the interpreted features from Figure 9 have been added.

2.3.2   Section WE 3

The 2009 GEORISK/USF 2D model, including the eastern portion, is shown in Figure 11. Shown in Figure 12 is the WesternGeco section WE 1 co-located on this 2D model from Figure 10. Again, note the opposite color scales between the 2D and 3D models. Also, Figure 12 shows three interpreted features, which are resistivity boundaries in the model, shown by the heavy dashed lines. These three interpreted features are shown directly on the 2D model in Figure 13 for comparison. As can be seen in these figures, there is reasonable correspondence between the 2D and 3D models.
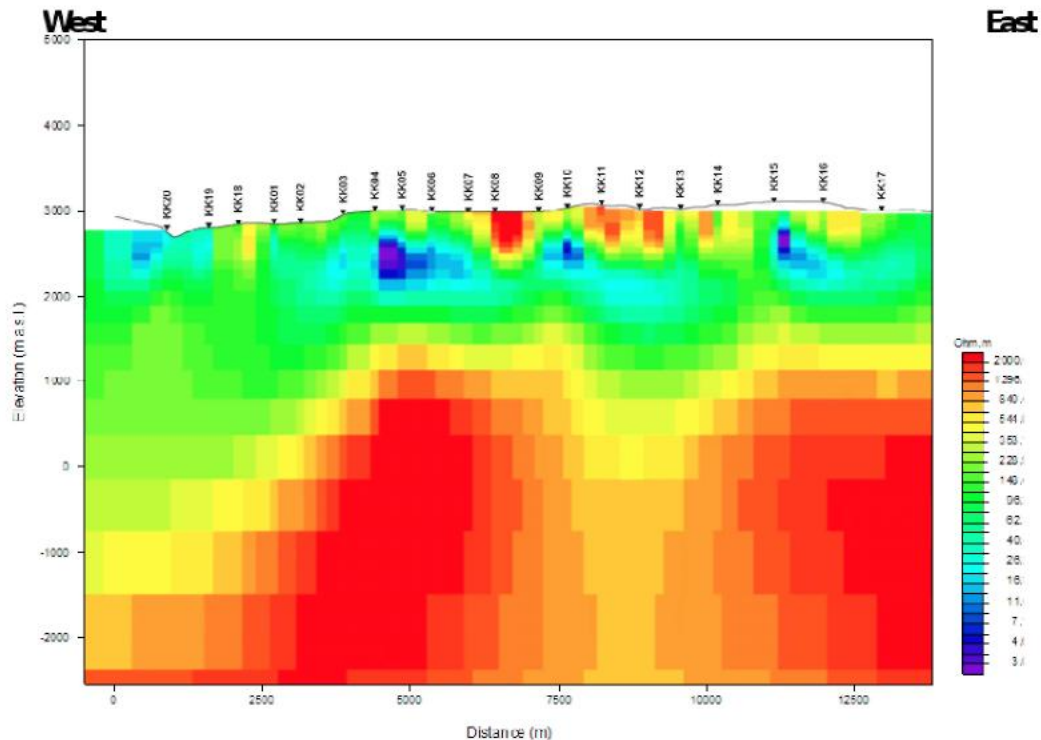
Figure 11: The 2009 GEORISK/USF 2D model, including its eastern portion. Note the resistivity color scale, which is thethe same on previous figures.

2.4 Re-Examination of the Pre-Existing Geothermal Model

We have shown that there is considerable agreement between the 2009 GEORISK/USF 2D MT model, and the 2011 WesternGeco 3D MT model, based upon our cross-sectional analysis. It has already been shown that the 2009 model is in agreement with models derived from the 2004 survey and subsequent 1D modeling. Therefore, we conclude that the WesternGeco model is valid, and in addition, due to the 3D nature of the modeling, which is stateof-the-art, the 3D model of subsurface resistivity more accurately depicts the resistivity distribution than previous works.

There is one caveat, however. The 3D model is considered more accurate only within the limits of the data that were used to derive it. For example, we showed that the resistivity basement on section WE 1 was extrapolated by the 3D modeling to continue to too shallow a depth toward the west, by comparison to the 2D model, which used data extending further in that direction. This difference is potentially important to hydrothermal flow models, because of the relative positions of the hot springs, borehole 4, and the fault-bounded graben, relative to this high resistivity zone.
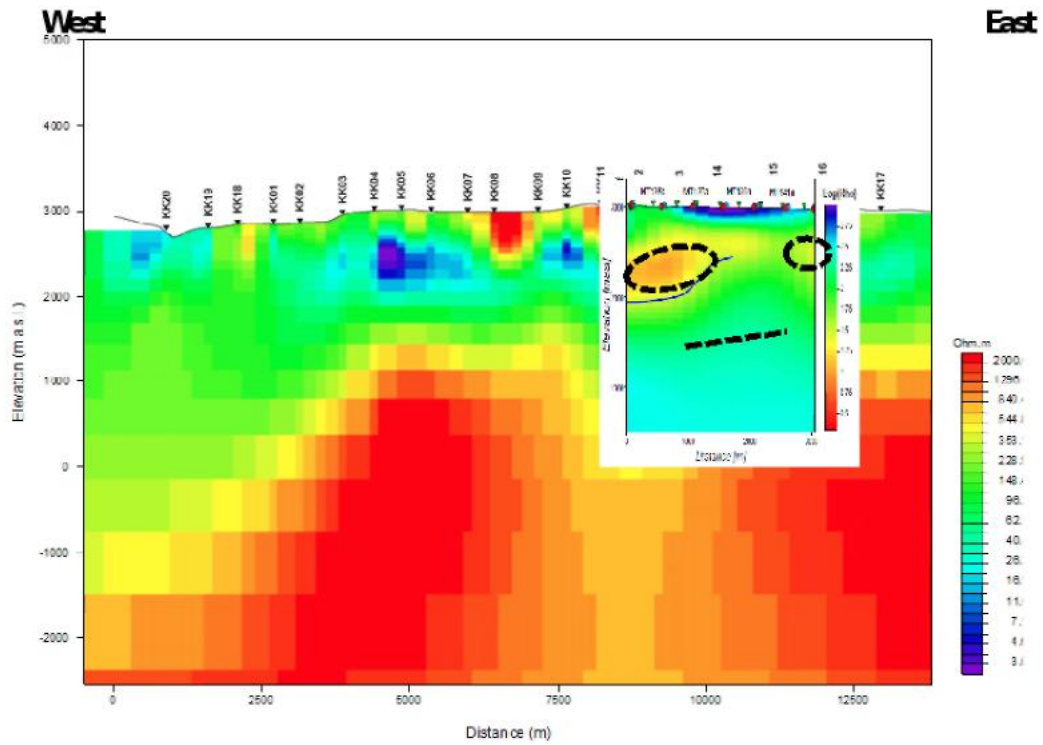
Figure 12: The 3D resistivity cross-section WE 3 is shown in its approximate position relative to the 2D model from Figure 11. Note that the resistivity color scales are opposite between the 2D and 3D models, as discussed in the caption for Figure 8. Also shown are three interpreted features as indicated by heavy dashed lines.
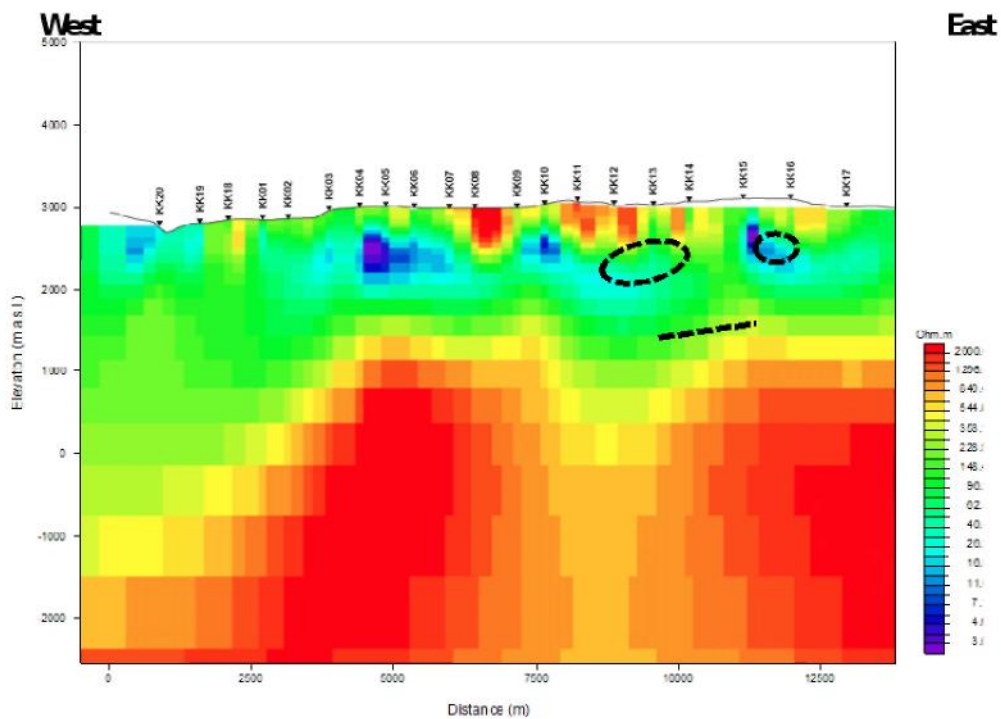
Figure 13: The 2D model from Figure 11 shown with the interpreted features, indicated by heavy dashed lines, from Figure 12.

The geothermal model to be tested by the 2011 data acquisition consisted of the pull-apart basin and associated faulting as shown in Figure 14. We have demonstrated that the WesternGeco 3D model is consistent with portions of the GEORISK/USF 2D model as shown in the background of the figure. The 3D model should provide detail of these structures toward the north and south of this model.

Figure 15 shows resistivity of the 3D model at an elevation of 1000 masl. Although the contour interval of the resistivity color intervals is quite broad, there is indication that a low resistivity anomaly exists in the west-central portion of the model (as indicated in the figure by Low Resistivity Zone A). This feature is bounded on the east and west by higher resistivity zones. The low resistivity anomaly at 1000 masl, is shown in the 2D model in Figure 16. There is obviously a difference in resistivity at depth between the 2D and 3D models. However, due to the greater coverage to the west in the 2009 MT survey used to generate the 2D model, it is likely that the western end of the 2D model is more accurate. The Higher Resistivity toward the west of the Lower resistivity zone in Figure 16 may be inaccurate.

As was stated previously, we believe the 3D model should be more accurate overall, and the previous geothermal model, illustrated in Figure 14, will require revision. Again, due to the way that the 3D model results have been presented, it is difficult to draw cross-sections of resistivity vs. depth for the 3D model.
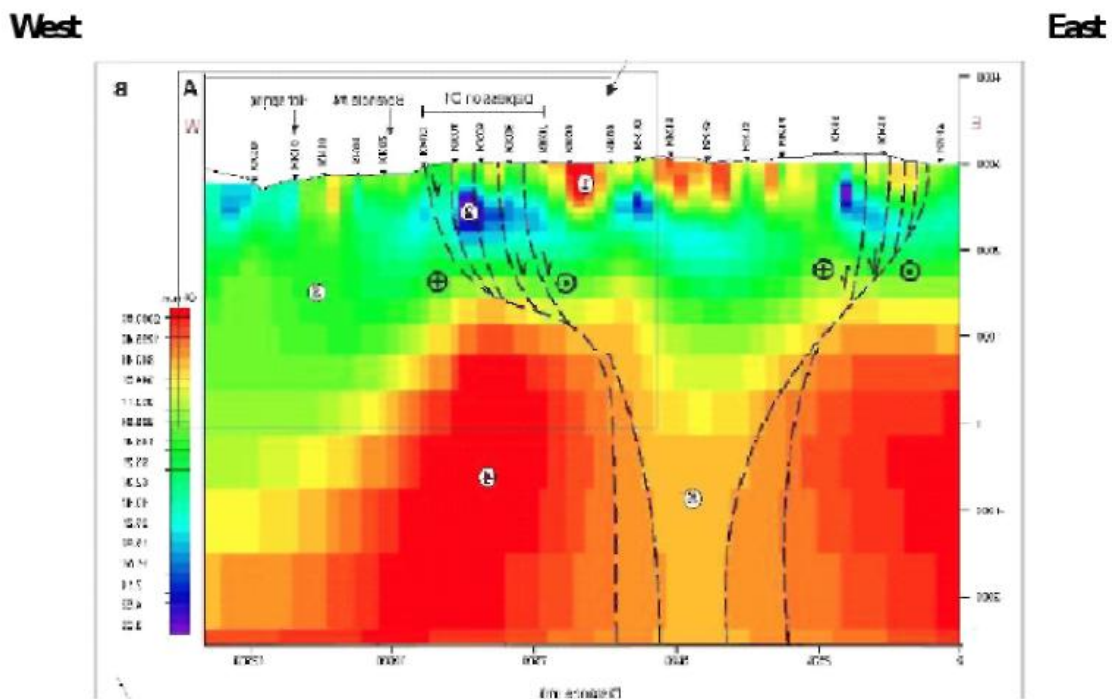
Figure 14: The 2D GEORISK/USF MT model with interpreted faults, reversed from Fig. 56, Report 29. These faults are associated with the pull-apart basin described in that report. The figure has been reversed to coincide with figures presented in the WesternGeco report.

Figure 15: The resistivity at 1000 m elevation, extracted from the 3D model (WesternGeco Report, Plate 2g, November 2011). Also shown is a low resistivity Zone A, as described in the text.
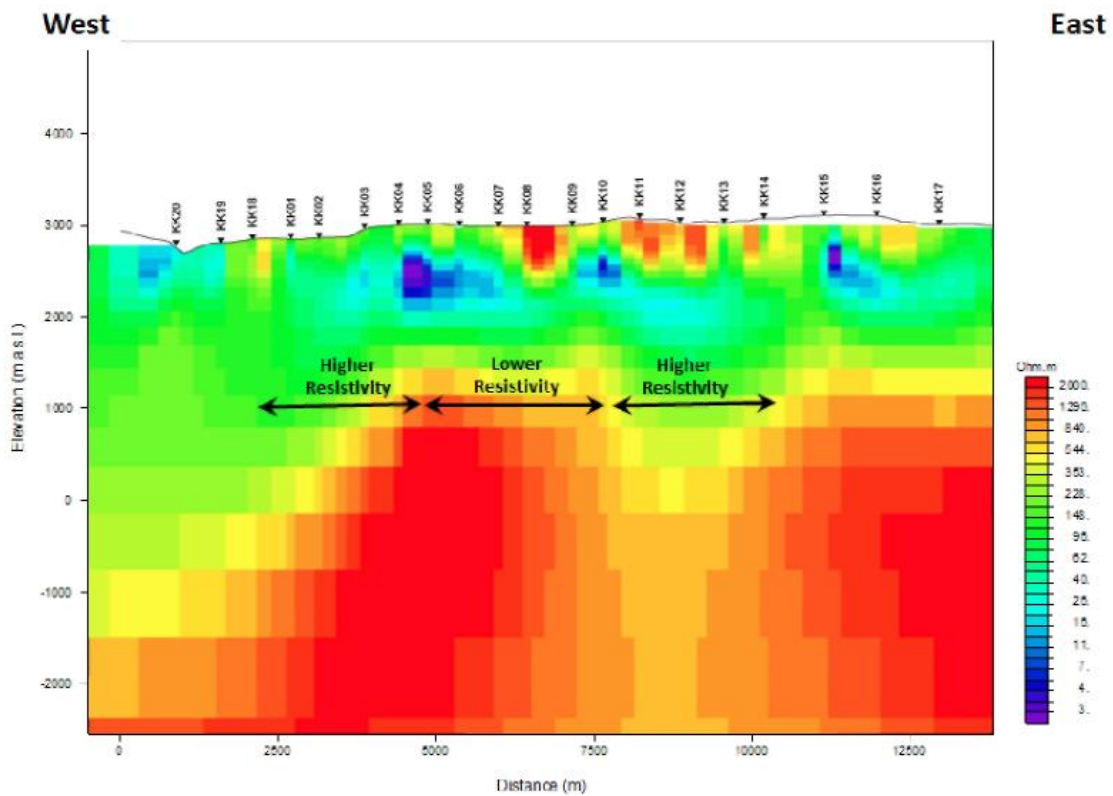
Figure 16: The 2D model showing where the discrepancies with the 3D model are at an elevation of 1000m. The region marked "Lower Resistivity" is the low resistivity Zone A in Figure 15.

2.5 Other Comments and Analysis Regarding the 3D Model

Referring back to Figure 5, and correlating locations of the 2004 MT survey with the 2009 MT survey positions shown in Figure 3, and locations of the 2011 MT survey positions shown in Figures 4 and 6, with relation to the 2009 survey, we can analyze the induction arrows from both 2004 and 2011.

Figure 17 shows tipper strike and induction arrows from the WesternGeco report. The region outlined by the red circle from their report is stated as anomalous, and is discussed briefly as an example of multi-dimensionality in the western portion of their survey. However, note that most of these arrows point toward the northeast, indicative of a conductive body toward the southwest. These arrows are computed from 100s data, which has a skin-depth of at least 15 km for the resistivities in this area. This is consistent with the low-resistivity at depth at the western portion of the 2D model, Figure 16. This is another indication that the 2D model may be more accurate in the west, toward the hot springs area.

Figure 18 shows resistivity of the 3D model at an elevation of 2000 masl. In addition, the figure shows a low-resistivity zone, labeled Zone B. It appears that this low-resistivity zone has some correlation with a topographic low. Many of the induction arrows shown in Figure 5, southwest of Zone B, are pointing away, toward the southwest also providing confirmation that the conductive region, ZoneB, is present. The 2004 data were computed at a period of 10s, yielding a skin depth of approximately 10 km, which is consistent with these analyses.

Therefore, we conclude this analysis of the 3D WesternGeco model and its relationship to the 2D GEORISK/ USF model from 2009. As previously stated, the 2004 modeling was shown to be consistent with the 2D GEORISK/ USF model.

Figure 17: Tipper strike and induction arrows at 100s (from the WesternGeco report (2011), Figure 3). Also shown is a red circle outlining an anomalous area, as stated in the WesternGeco report.
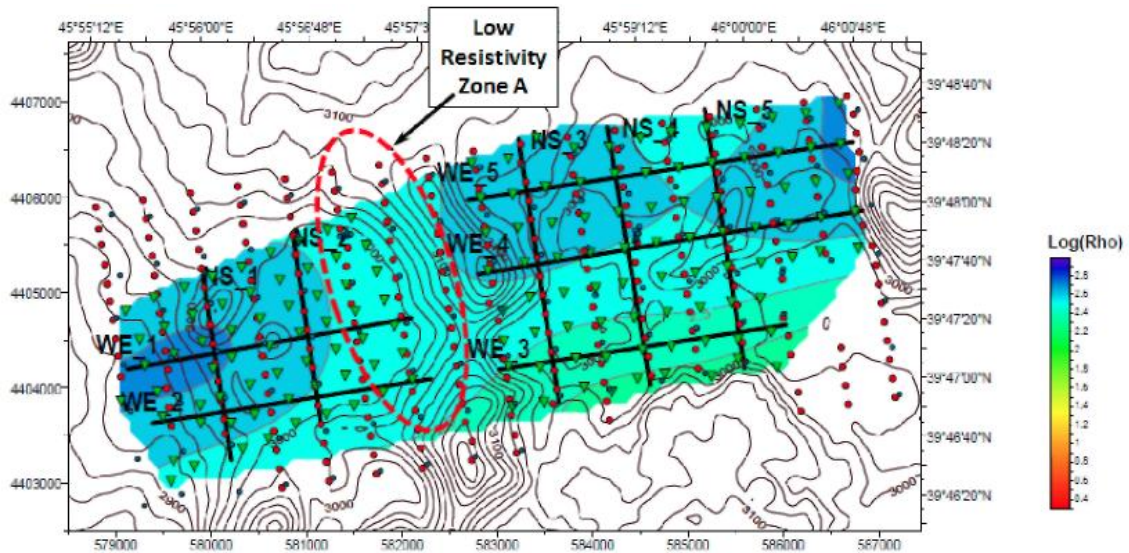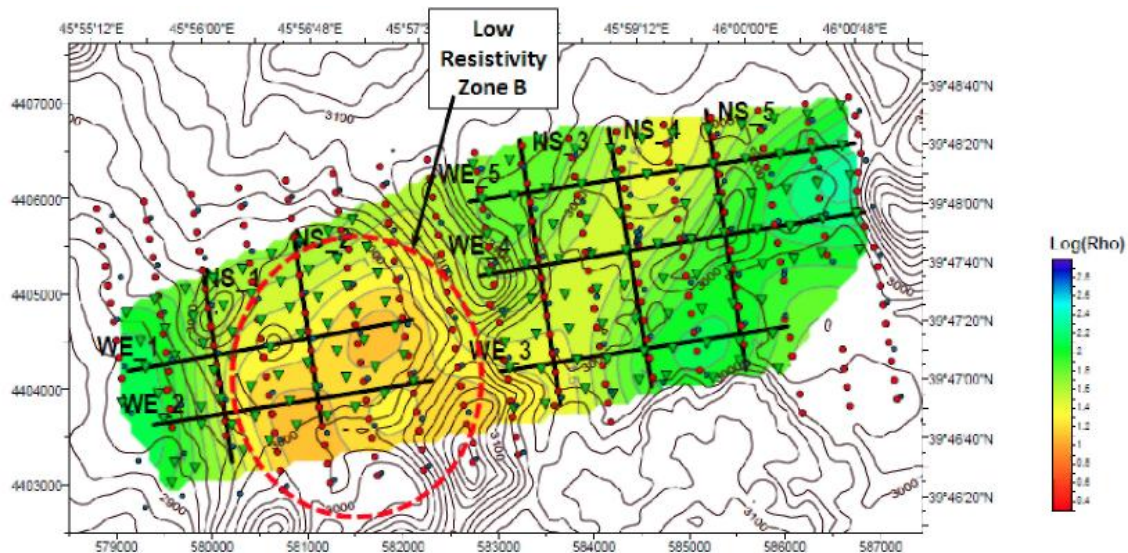
Figure 18: The resistivity at 2000 m elevation, extracted from the 3D model (WesternGeco Report (2011), Plate 2e). Also shown is a low resistivity Zone B, as described in the text.
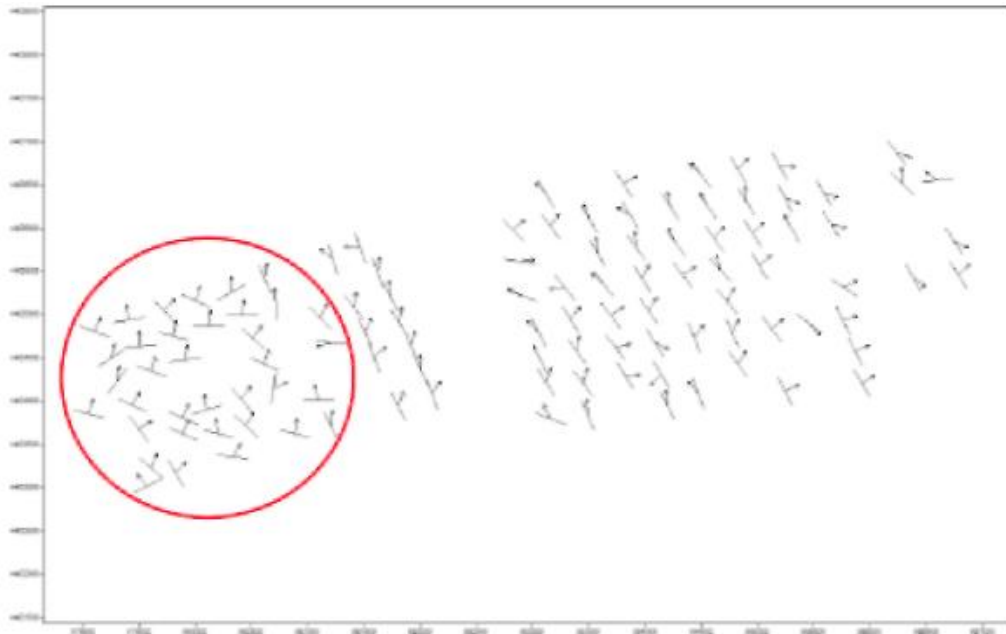
3. Gravity

3.1   Introduction

Gravity anomalies are created by geologic structures that create lateral discontinuities in the crust. For example, faults may juxtapose rocks of different densities and therefore gravity anomalies (e.g., a change in the gradient of the gravity field) are frequently associated with faults. Gravity measurements involve collection of data at individual gravity stations where both relative change in gravity and precise location (horizontal and vertical) are determined. For the Kar Kar geothermal assessment, WesternGeco performed a gravity survey on a grid over a comparatively small area within the major area of interest. The goals of making this gravity map were to (i) identify geological discontinuities associated with potential fault-bounded basins, (ii) provide data to constrain the depth(s) of basins in the survey area, a key parameter for understanding the circulation and heating of groundwater, and (iii) compare gravity anomalies (and the resulting models) with resistivity anomalies identified as part of the 3D magnetotelluric (MT) survey and modeling effort. The primary origin of gravity anomalies in the region is related to the density contrast between quartz monzonite identified in Borehole4 and the lava flow and alluvial package that fills the fault-bounded basin mapped within the survey area.

The WesternGeco gravity observation dataset included 257 gravity measurements and individual stations collected by WesternGeco. The data were collected on an approximately regular grid (Figure 19). The apparent low gravity anomaly is likely a result of low density sediment and relatively low density lava flows infilling the valley created by N–S trending basin-bounding faults, which juxtaposes quartz monzonite or related basement rocks against these lower density rocks. In the following, we:

19

1. Review the WesternGeco sampling procedures

2. Complete gravity reductions using the WesternGeco dataset and a variety of Bouguer densities, and compare the results with topographic features, thereby identifying an appropriate range of Bouguer densities for the modeling effort

3. Perform a high-dimensional gravity inversion of the WesternGeco dataset using a variety of Bouguer densities in order to construct a geological model of the basin

4. Compare the model results with MT results and discuss the impact of the model and comparison on development of the hydrothermal model
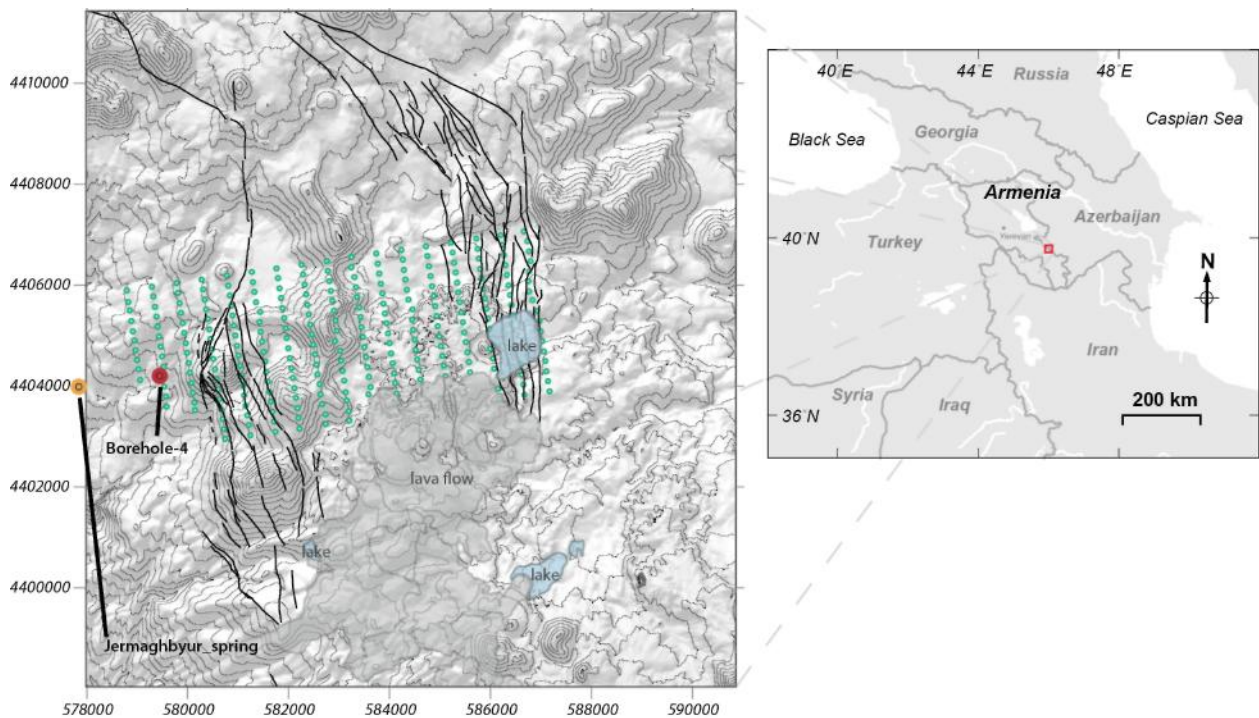
Figure 19: Gravity station locations for the survey grid created by WesternGeco staff (solid circles). Mapped faults shown as heavy solid lines; topography is contoured with light solid lines; superimposed on shaded relief DEM. Borehole 4 (solid red circle) lies within the western portion of this grid. Lakes and a young (Holocene?) lava flow are also shown. The hot springs lie west of the grid. UTM projection WGS84.

3.2   Gravity Data

Gravity data were collected by WesternGeco during gravity surveys in summer, 2011. Review of field procedures indicates that WesternGeco staff did an excellent job of high-resolution gravity data collection. Instrument drift appears to have been minimal. High vertical precision on elevation of gravity stations was achieved. Although the report does not provide details of the terrain correction, specifically about the way local terrain differences were incorporated into the digital terrain model (DEM) based correction, the WesternGeco approach appears to have been reasonable (resulting in terrain corrections generally < 1 mgal Figure 20.

3.3   Gravity Reductions

Gravity reductions, and particularly the choice of density for the Bouguer corrections, have an important impact on modeling. WesternGeco staff used a density of 2700 kg m^{-3} for the Bouguer density. This is higher than values normally used in gravity modeling, especially for local gravity surveys, and may lead to correlation between modeled geological features and topography, as noted in the WesternGeco report. In fact, inspection of Figure 20 does indicate that some correlation occurs, especially with the N-S trending low gravity values and the topographic ridge in the central part of the map area. Therefore, we undertook to repeat the gravity reduction using a variety of Bouguer densities, using data provided in the WesternGeco report, in order to assess the impact of this assumption (Bouguer density of 2700 kg m^{-3}) on model results.

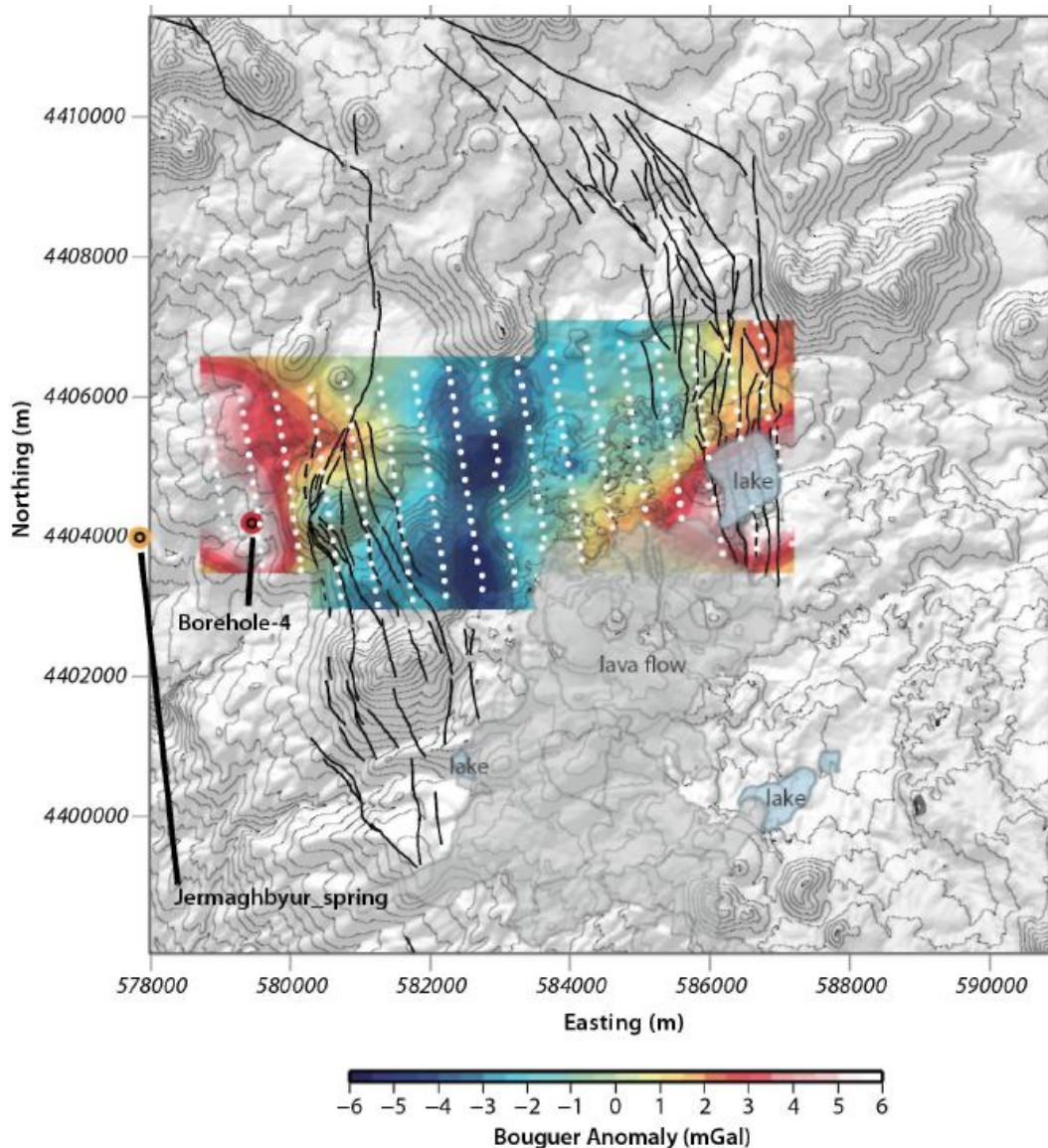**Figure 20:** Complete Bouguer anomaly mapped by WesternGeco staff (color shaded region). Mapped faults shown as heavy solid lines; topography is contoured with light solid lines; superimposed on shaded relief DEM. Borehole 4 (solid red circle) lies within the western portion of this grid. Lakes and a young (Holocene?) lava flow are also shown. The hot springs lie west of the grid. UTM projection WGS84.

Drift and Tidal Corrections WesternGeco staff report low instrument drift, thought to be linear during the sampling period. The gravity instrument used performs tidal corrections automatically, using the Longman formulas. We did not have the information, or think it necessary, to repeat drift and tidal corrections.

Theoretical Gravity (mGal) Gravity varies with latitude due to the change in diameter of the Earth with latitude and change in angular acceleration with latitude. The change of gravity with latitude is the theoretical gravity. We use the Somigliana closed-form solution to estimate theoretical gravity:

$$g_T = \frac{g_e(1 + k\sin^2\phi)}{(1 - e^2\sin^2\phi)^{\frac{1}{2}}},$$

(1)

where g_T, is the theoretical gravity on the GRS80 reference ellipsoid at latitude ϕ, g_e is normal gravity at the equator equal to 978032.67715 mGal, k is a dimensionless derived constant equal to 0.001931851353, and e being the first numerical eccentricity with e^2 having a value of 0.0066943800229.

Free Air Correction (mGal) The difference in elevation between the base station and the measurement point results in a difference in gravitational acceleration. The free air correction is applied to account for difference in gravity due to difference in measurement height. For the GRS80 ellipsoid the second-order formula for the precise free air correction is:

$$\delta g_h = -(0.3087691 - 0.0004398 sin^2\phi)h + 7.2125 \times 10^{-8}h^2;$$

(2)

where the free air correction, δg_h, is calculated in milligals and h is the elliptical elevation of the gravity station measured in meters.

Atmospheric Correction (mGal) The weight of the atmosphere varies with height and this change affects gravity measurements. The atmospheric correction accounts for the change in weight of the atmosphere between the base station and the measurement point. The formula for the atmospheric correction is:

$$\delta g_{atm} = 0.874 - 9.9 \times 10^{-5}\,h + 3.56 \times 10^{-9}\,h^2\,,$$

(3)

where the atmospheric correction, Sg_{atm}, is given in milligals and h is the elliptical elevation of the gravity station in meters.

Bouguer Correction (mGal) The Bouguer correction accounts for the mass of average crust between the base station and the measurement point, given the height difference between them. The Bouguer correction used here accounts for the spherical cap-shape of this mass of rock, as described in LaFehr (1991). The formula for the Bouguer correction is:

$$g_{sc} = 2\pi G\rho[(1 + \mu)h - \lambda R],$$

(4)

where g_{sc} is the gravity correction due to the spherical cap in milligals, ρ is the density of the material making up the spherical cap, μ and λ are dimensionless coefficients, and $R = R_0 + h$, where R_0 is the mean radius of the Earth and h is the elevation of the gravity station on the reference ellipsoid.

Terrain Correction (mGal) The free air and Bouguer corrections incompletely account for topographic effects on gravity measurements. The terrain correction accounts for differences produced by actual terrain and required DEM to implement. WesternGeco performed terrain corrections using a DEM and elevation differences measured near each gravity station, using a Bouguer density of 2700 kg m^{-3}.

We are uncertain from the WesternGeco report exactly how the terrain correction was computed. Normally, the inner zone correction accounts for topographic variation within Hammer's zone C, <53.3m from the gravity station, and is computed using the quarter-wedge method described by Nowell (1999), an improved version of the power-law approximation method of Campbell (1980). The intermediate zone correction is normally performed for DEM grid points that fall between Hammer's zone D, >53.3m, and outer radius of Hammer's zone K, 9903 m. This terrain correction is done using the simplified gravity attraction of a prism approximated as an annular ring, described by Kane (1962). The far-field terrain correction is usually performed for topographic variation >9903m and up to the extent of the input DEM (if SRTM-derived DEM is used, up to 163 km). This far-field correction is carried out by means of the vertical line mass approximation described by Blais and Ferland (1984), which is the approximation of the gravity attraction due to a prism in the far-field.

Recalculation of the Gravity Reduction. We recalculated the gravity reduction using equations 1 – 4. Through this procedure we verified the complete Bouguer gravity anomaly presented by WesternGeco staff in their report, using a Bouguer density of 2700 kgm^{-3}. Because we are most interested in the local variation in the gravity field (i.e., within the boundaries of the survey area), a residual gravity anomaly was computed by subtracting the complete Bouguer anomaly (the anomaly obtained after the application of the terrain correction) from an assumed regional trend, estimated by fitting a plane to the complete Bouguer anomaly map using the generalized least-squared method (Figure 21). Inspection of Figure 21 indicates that there is some correlation of the complete Bouguer gravity anomaly with topography, especially indicated by the low gravity values associated with a topographic ridge that extends N–S through central part of the map area. This correlation with topography suggests that the Bouguer density of 2700 kgm^{-3} is high, and that lower Bouguer densities are more appropriate for use in modeling the local gravity anomaly. This is important because the choice of the Bouguer density affects the estimated basin depth derived from the gravity data, a key parameter in the hyrothermal model.

We note that much of the topography around the site is due to emplacement of lava flows. There are few measurements of bulk lava flow density reported in the literature. In Hawaii, basalt density measurements in boreholes were 2000‒3000 kg m^{-3}, with mean value of 2500 kg m^{-3} for water saturated lava flows (Moore, 2001). Thus, although basalt samples have densities on order 2700‒3000 kg m^{-3}, the bulk density of lavas is less due to the presence of fractures and flow vesiculation. Kar Kar lava flows should be close to this density, or perhaps slightly less for partially saturated rocks that form topographic highs in the local survey area.

Therefore, we recomputed the gravity reduction, using a range of lower values of the Bouguer density, 2200 kg m-^{3} < ρ < 2700 kg m-^{3} . We used the terrain corrections computed by WesternGeco using 2700 kg m^{-3} because terrain information, especially for the inner Hammer zone, was not available to us. This leads to a very slight over-correction for terrain effects when lower Bouguer densities are used. However, we note that the error introduced into the terrain correction is very slight (<< 1mgal), and therefore not meaningful compared with the amplitude of the computed anomaly.
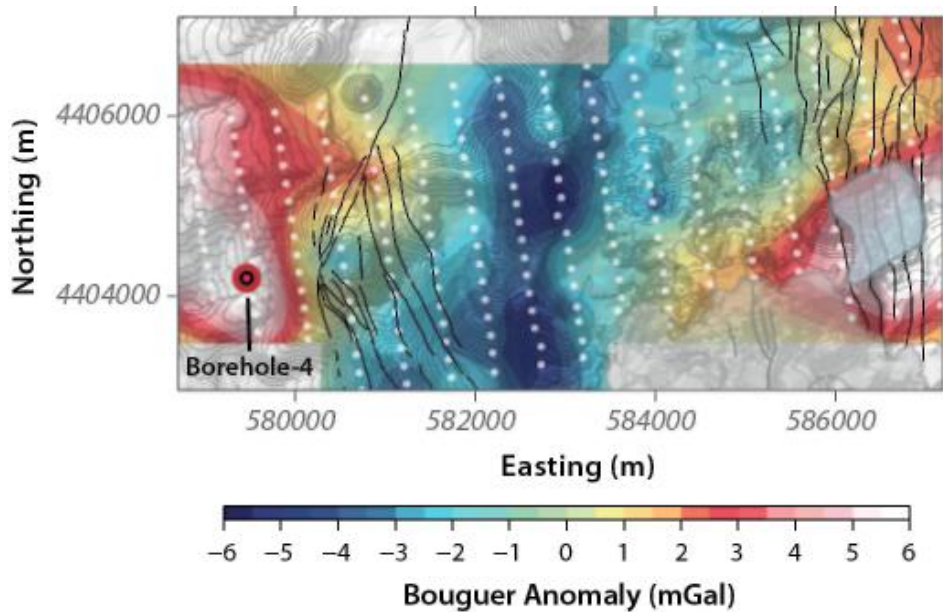
Figure 21: Complete Bouguer gravity anomaly (color-shaded) calculated using a density of 2700 kgm^{-3} and with a best-fit plane subtracted. Note the correlation of gravity anomalies with topography (contour lines) indicating this Bouguer density is high. Mapped faults shown as solid lines; gravity stations shown as solid circles; superimposed on shaded relief DEM. UTM projection WGS84.

Figures 22, 23, and 24 show example results of this re-computation using lower Bouguer densities, each time subtracting the best-fit plane from the data. Inspection of these maps shows that correlation with topography is minimized using Bouguer densities of 2300 kg m^{-3} < ρ < 2550 kg m^{-3}. For lower Bouguer densities (e.g., ρ = 2200kgm^{-3}), an anti-correlation with topography emerges. In the following, we construct a forward model using a complete Bouguer anomaly calculated with a Bouguer density of 2550 kg m^{-3}, acknowledging that slightly lower values may also be used.
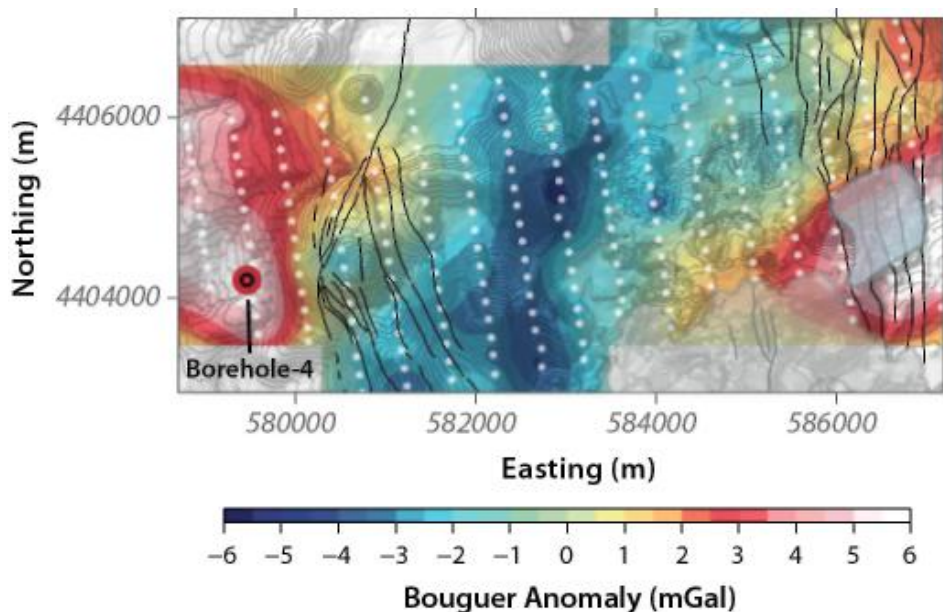

Figure 22: Complete Bouguer gravity anomaly (color shaded) calculated using a density of 2550kgm^{-3} and with a best-fit plane subtracted. This complete Bouguer gravity reduction was selected for modeling. Other map symbols as in Figure 21.
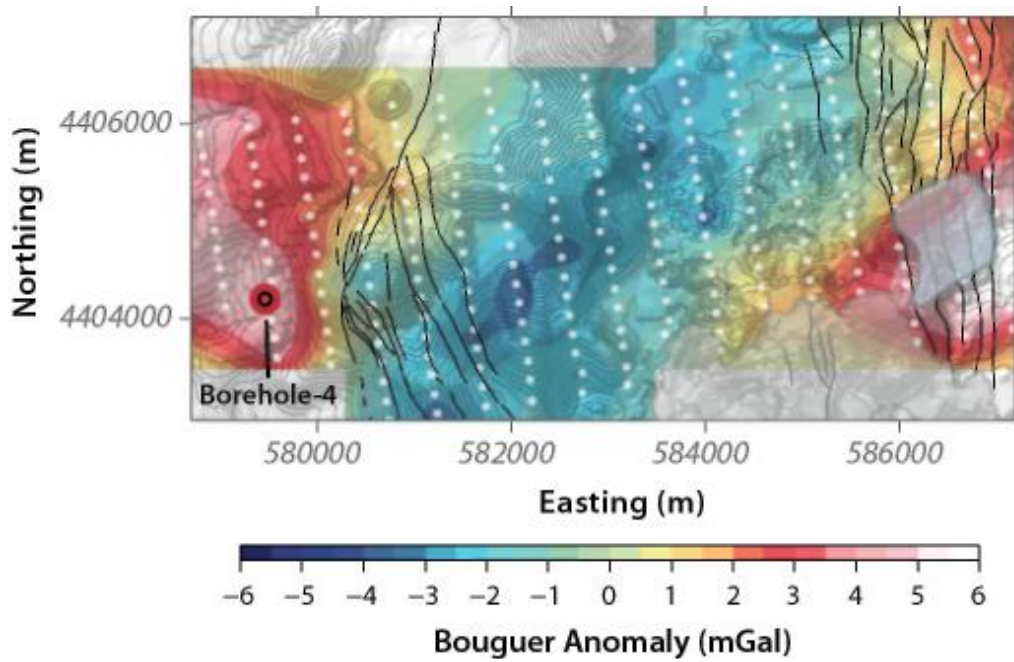
24

Figure 23: Complete Bouguer gravity anomaly (color shaded) calculated using a density of $2300 \mathrm{kgm}^{-3}$ and with a best-fit plane subtracted. This complete Bouguer gravity is not well correlated to topography, indicating that this Bouguer density is acceptable for modeling. Other map symbols as in Figure 21.
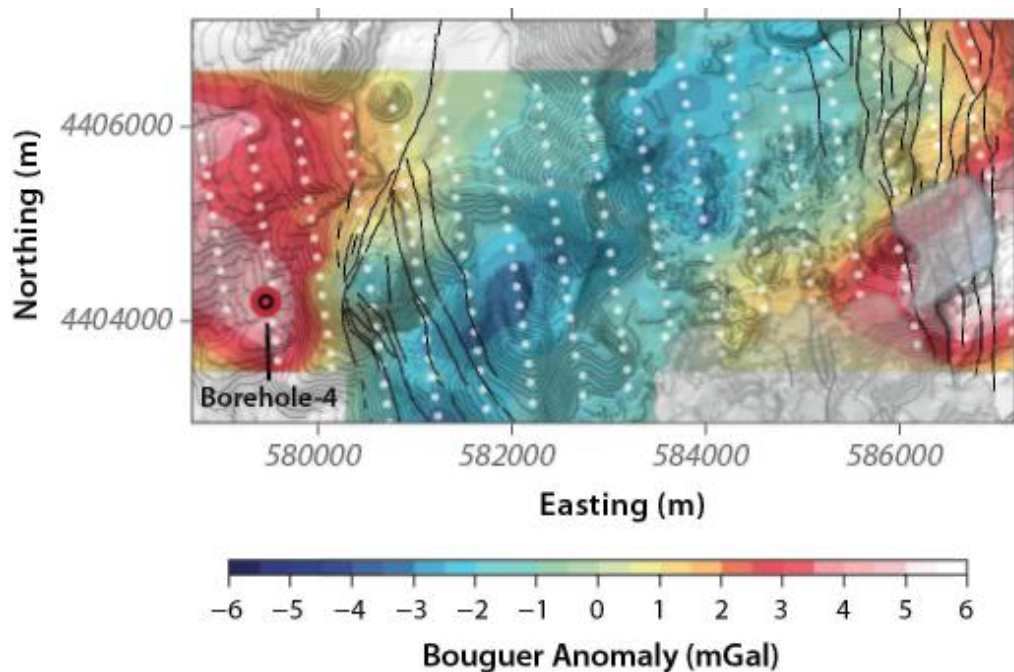

Figure 24: Complete Bouguer gravity anomaly (color shaded) calculated using a density of $2200 \mathrm{kgm}^{-3}$ and with a best-fit plane subtracted. This complete Bouguer gravity is anti-correlated to topography, indicating that this Bouguer density is relatively low. Other map symbols as in Figure 21

3.4   Gravity Forward Model

The forward gravity model consists of 6603 rectangular prisms aligned in a uniform grid, which is approximately centered on the dataset of observed gravity stations (Figure 19). Each rectangular prism is 200 meters square in the horizontal plane. Each prism extends from the surface to some depth, inferred through the inversion. The depth of each prism is adjusted during the inversion process to minimize differences between the observed complete gravity field and the calculated gravity field.

For this inversion, the density contrast of each prism was fixed at a value of $-250.0 \mathrm{kgm}^{-3}$, which is assumed to represent the bulk density contrast for the valley-fill sediments, volcaniclastics and low density lava flows with the underlying quartz monzonite or comparable basement. Using the Bouguer density of 2550 kg m^{-3}, this implies a density for the quartz monzonite of 2800 kg m^{-3}, which is generally taken to have a normative bulk density (unfractured) of approximately 2770 kg m^{-3} (Daly, 1935). Thus, given the uncertainties in the density of the alluvium and lava flow in-filling the basin, a model density contrast of $-250.0 \mathrm{kgm}^{-3}$ appears to be appropriate.

3.5   Gravity Inversion

The Gauss-Newton procedure with the Levenburg-Marquardt modification was used to invert the gravity data for the depth distribution. This depth distribution represents the depth to the quartz monzonite, given a uniform package of basin-filling sediments and lava flows. Pilot points were used as a parameterization device to reduce the dimensionality of the inverse problem, while maintaining maximum degrees of freedom. The pilot points were distributed non-uniformly throughout the forward model domain, focused near the gravity stations (Figure 25). A total of 431 pilot points were used to parameterize the depth distribution of the forward model grid.

Constructing an inverse problem with more degrees of freedom than observations is an under-determined problem. Solving this type of problem requires finding a psuedo-inverse solution that meets the Moore-Penrose conditions, which is found using singular value decomposition (SVD) in combination with Tikhonov regularization. Although the SVD and regularization result a numerically tractable problem, inverting for more parameters than data requires the specification of an acceptable level of data error, or misfit. Otherwise, overfitting of the data, which include noise from various sources, will occur. The goal of the inversion process is then to find a minimum of regularization error at the specified level of data error or misfit. Different values of acceptable misfit produce different solutions to the inverse problem. Ideally, if the observation errors are assumed to be normally distributed and the forward model does not produce any structural error (and the co-factor matrix is the identity matrix), then the acceptable level of misfit should be the product of the standard deviation of the observation error and the number of observations.

To explore the trade-off between assumed observation error and regularization error, the inversions process is wrapped in a multi-objective framework. The result is a series of solutions to the inverse problem for unique combinations of minimized regularization error and data misfit. These unique combinations are known as Pareto optimal points and the collection of these points forms the Pareto frontier, which quantitatively defines the trade-off between the two competing objectives.
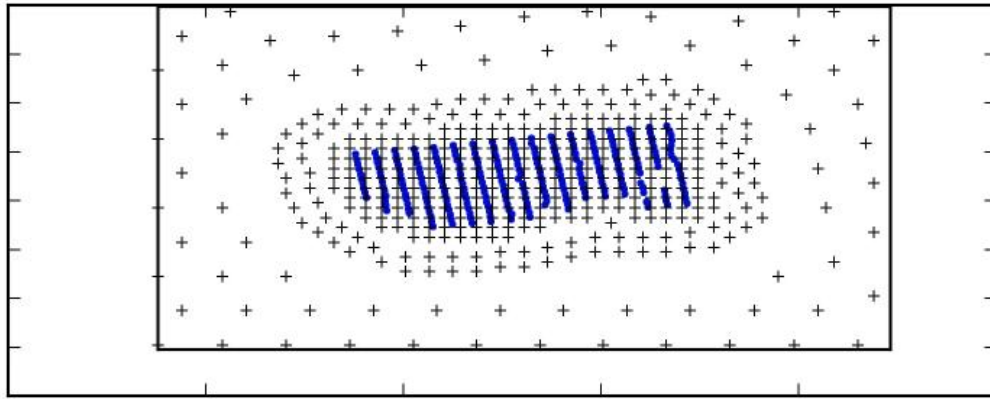
Figure 25: Location of pilot points (black crosses) and gravity stations (blue points) within the forward model domain

3.6 Gravity Model Results

Ten Pareto optimal points were found for a range of assumed observation error standard deviation (Figure 26).The resulting depth distribution, as well as a comparison of observed and simulated gravity response are presented in the Appendix of this report.

Assessment of the Pareto plot suggests that an error model standard deviation of 0.3 to 0.4 mgals results in an equitable trade-off between misfit and plausibility (points 4 or 5 on Figure 26). In other words, the inversion does not attempt to refine models to less than this range of values, reflecting both uncertainty in the true value of gravity at observation points and additional complexities of the gravity anomaly distribution, not accounted for in the forward model.
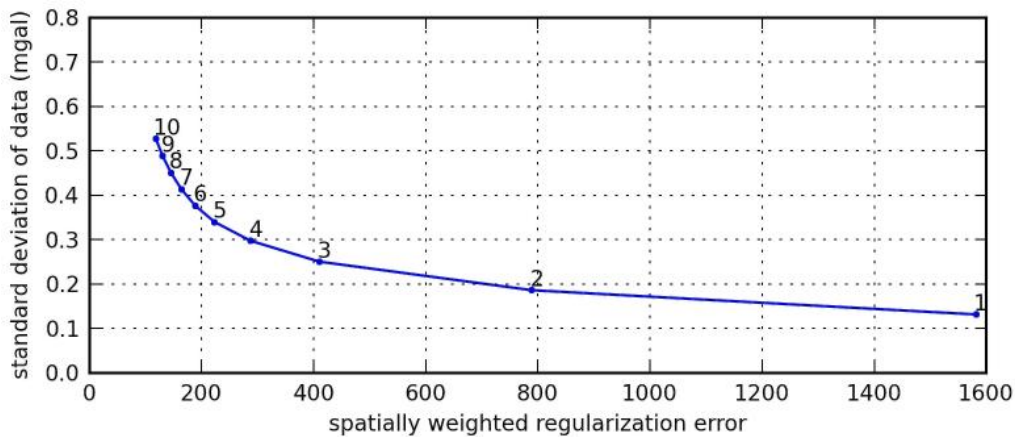
Figure 26: The Pareto frontier between assumed observation error standard deviation and regularization error.

Model depths are shown in Figure 27 and the forward solution to the gravity calculation based on this model is shown in Figure 28. Although strong constraints are placed on the model because only one density contrast is used, it is clear that relatively smooth variation in basin-fill can model the observed variation in gravity. The major feature of the model the presence of a narrow N–S trending basin through the center of the map area, reaching a maximum depth of approximately 1500m and bounded by mapped faults. We note that the model depth at the western margin of the gravity grid, nearest borehole 4, is approximately 150m, in excellent agreement with the depth measured to the top of the quartz monzonite in the borehole (123 m).
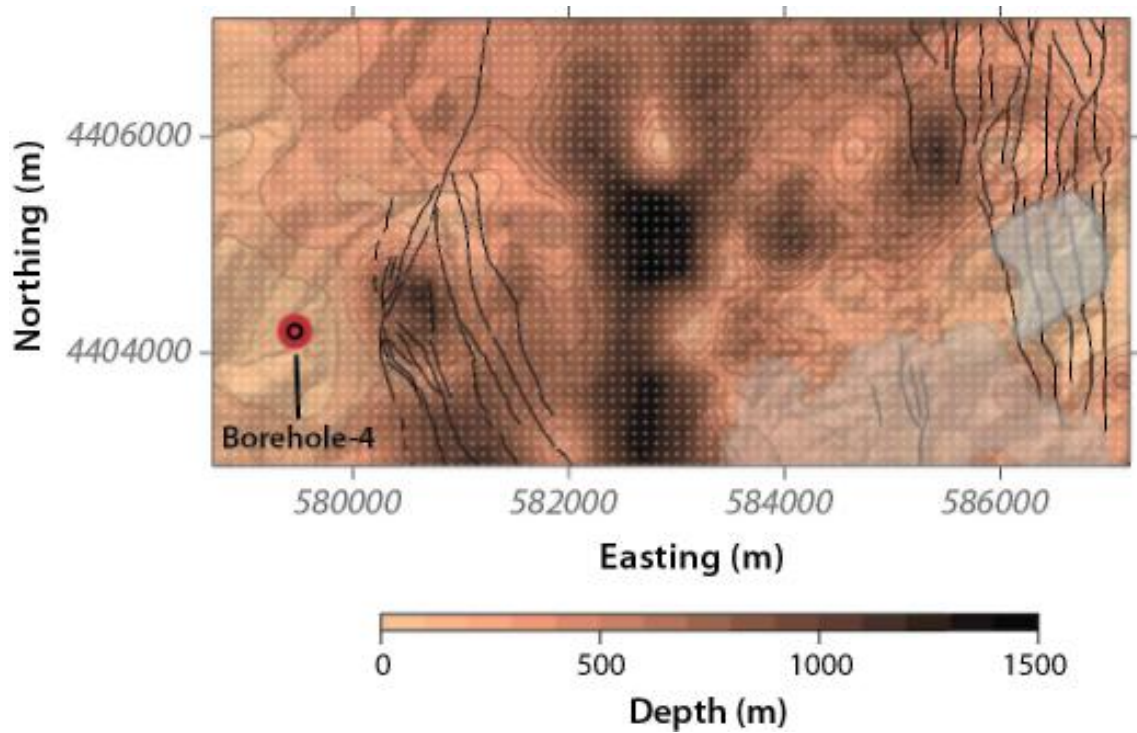
Figure 27: Depth distribution of base of basin-fill (lavas, alluvium, volcaniclastics), and top of basement (quartz monzonite?) in the survey area based on inversion of the gravity anomaly with Bouguer density 2550kgm^{-3}. Small solid circles indicate the positions of centroids of model prisms. Other symbols as in Figure 21.
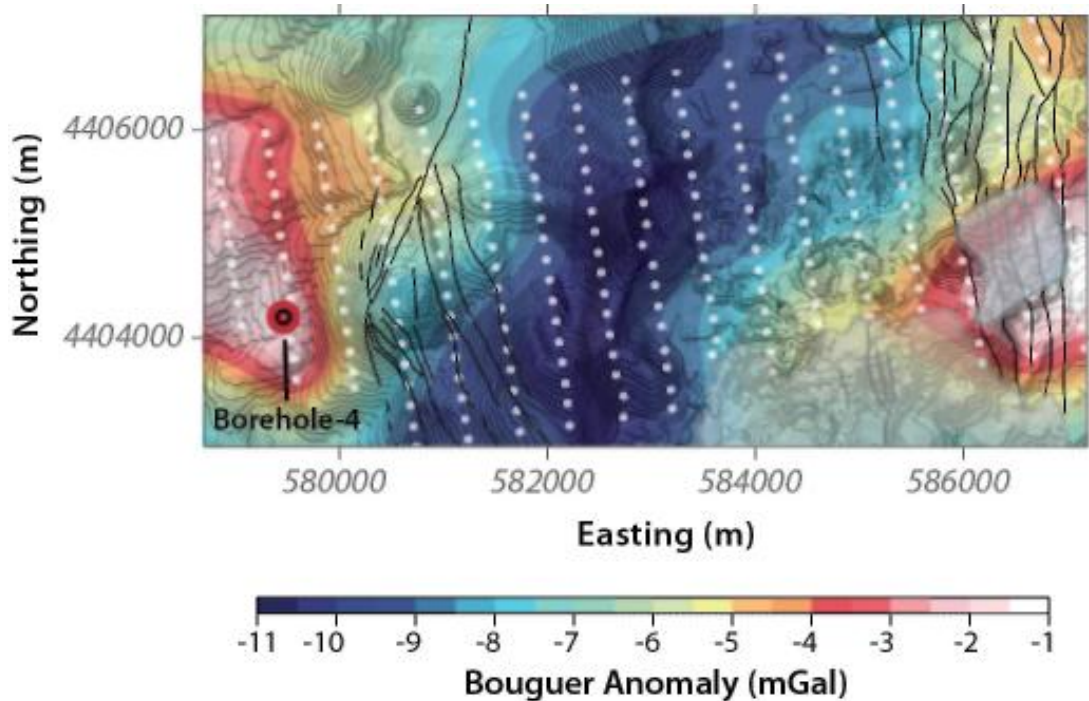

Figure 28: Forward model of the gravity anomaly calculated using the depth model shown in Figure 27. All other map symbols as in Figure 21.

4. Geothermal Model

The geophysical data and models based on interpretation of these data place important constraints on the hydrothermal model for the Kar Kar area. The geophysical models also are consistent with observations made in borehole 4 (Figure 29).

Interbedded lavas and alluvium occur in borehole4 to a depth of 123m. Quartz monzonite was logged from 123m to the bottom of the hole at approximately 1000m depth. The thickness of alluvium and lava flows derived from the gravity model in the westernmost portion of the grid, east of borehole 4, is approximately 150m. This suggests that the model depths from the 3D inversion of gravity data represent the depth to basement, which at least in borehole 4, is quartz monzonite.

The quartz monzonite in borehole 4 is variably fractured. A water-bearing zone was identified through interpretation of the temperature log (Figure 29) at a depth of approximately 340m. Temperatures of water in this zone in borehole4 were 30-35°C, the same temperature as the Jermaghbyur hot springs. Both the 2D MT model (GEORISK/USF, 2009) and the 3D MT model (WesternGeco, 2011) identify a prominent low resistivity zone east of borehole 4 at approximately this depth. Hot fluids within a fracture zone can explain this low resistivity anomaly. It seems possible that fracture flow through the quartz monzonite rapidly delivers hot water to the springs by predominately lateral transport through this water-bearing zone from the area of the low resistivity anomaly.
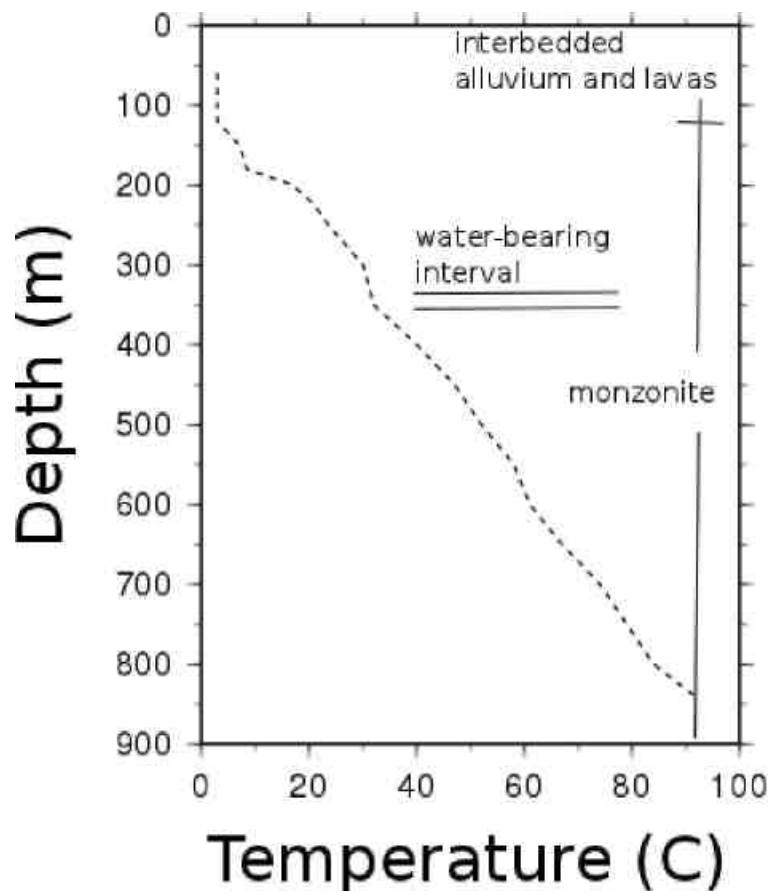
Figure 29: Temperatures logged in borehole 4. A water-bearing zone corresponds to isothermal conditions at a depth of approximately 340 m. Interbedded alluvium and lava flows were reported in the well at depths less than 123m; quartz monzonite occurs in the well from 123 m to its total depth, approximately 1000 m.

The low resistivity anomaly appears to be thickest and of greatest amplitude at the projected location of steeply dipping faults bounding the western edge of the N–S trending basin. The 3D gravity model suggests that this basin rapidly deepens to approximately 1500 m east of the low resistivity anomaly. Additional low resistivity anomalies, although of lower amplitude, are identified in the 3D MT model within the basin.

Both the 2D MT model (GEORISK/USF, 2009) and the 3D MT model (WesternGeco, 2011) identify an increase in resistivity at a depth of approximately 1500 m beneath the low resistivity zone adjacent to the borehole. This transition may represent a change from water saturated fractured quartz monzonite to unfractured rock, and hence impermeable, rock at greater depth. The MT results from 2009 and 2011 are somewhat inconsistent about whether this zone shallows or deepens to the west. It appears that this zone deepens within the basin based on 2009 MT modeling results.

Finally, the geothermal gradient measured in borehole 4 is clearly anomalous, reaching approximately 100°C km^{-1} in the lower half of the well. The quartz monzonite is reported to be fractured in zones throughout much of the well. The anomalous temperature gradient, the presence of fractured igneous intrusion, and the presence of the narrow N–S trending basin within the survey area all create conditions for rapid transport of hot water from within the basin from depth to the surface along permeable fractures. It is possible that this fracture flow is partially controlled by faults bounding the western margin of the basin. The water-bearing zone at 340m depth in the well may represent a mixing zone between these up-welling fluids and meteoric recharge.

Our interpretation is that the major features of gravity and MT modeling, along with the borehole observations, indicate that meteoric water may circulate to substantial depth within the basin. A heat source at depth is required to explain the anomalous geothermal gradient in borehole 4. It is uncertain if this heat source is localized within the fault-bounded basin, or is larger, for example extending to the west.

Blais, J. A. R. and Ferland, R. (1984). Optimization in gravimetric terrain corrections. *Canadian Journal of Earth Sciences,* 21:505–570.

Campbell, D. L. (1980). Gravity terrain corrections for stations on a uniform slope – a power law approximation. *Geophysics,* 45:109–112.

Daly, R. (1935). Densities of rocks calculated form their chemical analyses. *Proceedings of the National Academy of Sciences,* 21:657–663.

Kane, M. F. (1962). A comprehensive system of terrain corrections using a digital computer. *Geophysics,* 27:455–462.

LaFehr, T. R. (1991). Standardization in gravity reduction. *Geophysics,* 56:1170–1178.

Moore, J. G. (2001). Density of basalt core from hilo drill hole, hawaii. *Journal of Volcanology and Geothermal Research,* 112:221–230.

Nowell, D. A. G. (1999). Gravity terrain corrections – an overview. *Journal of Applied Geophysics,* 42:117–134.
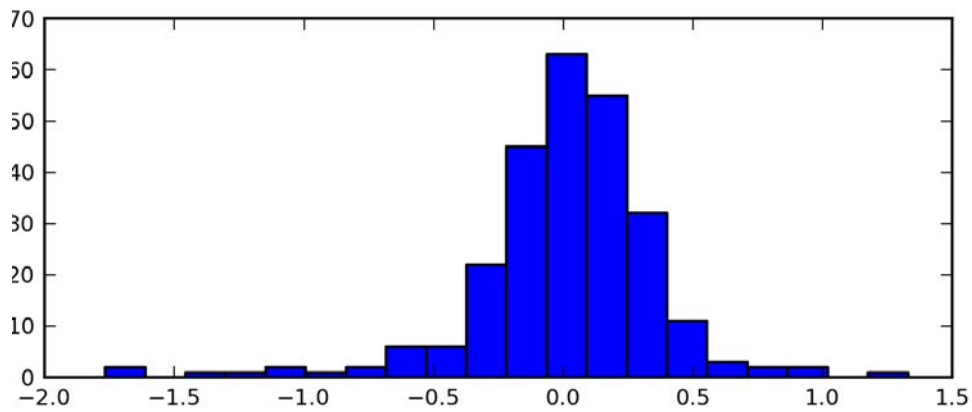
5. Appendix 1

Gravity inversion results using a Bouguer density of 2700 kgm^{-3} for different Pareto points.
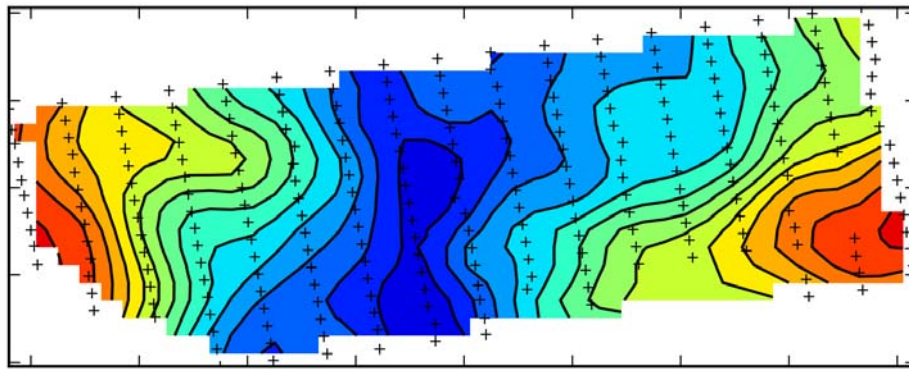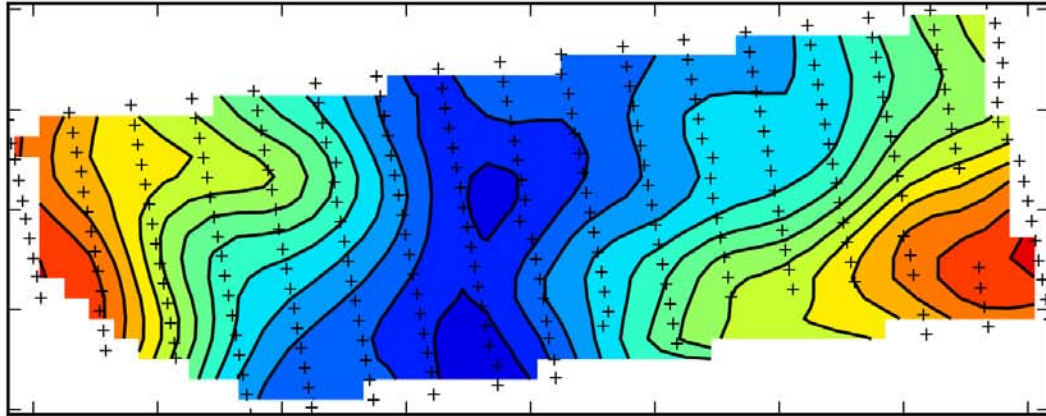

(a) simulated gravity response
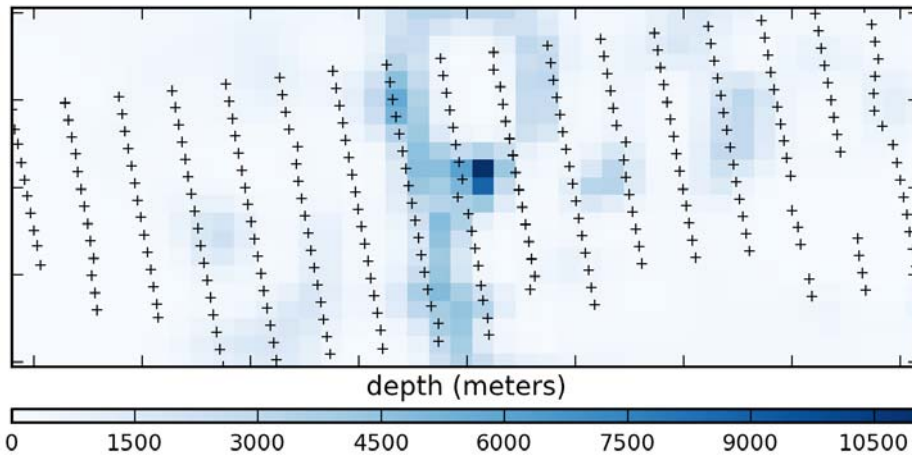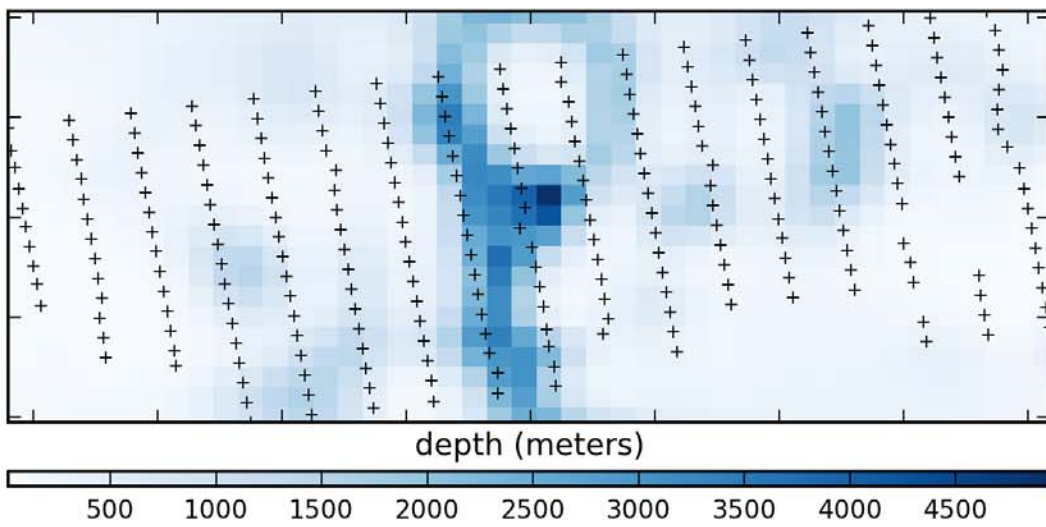

(b) inverted depth distribution
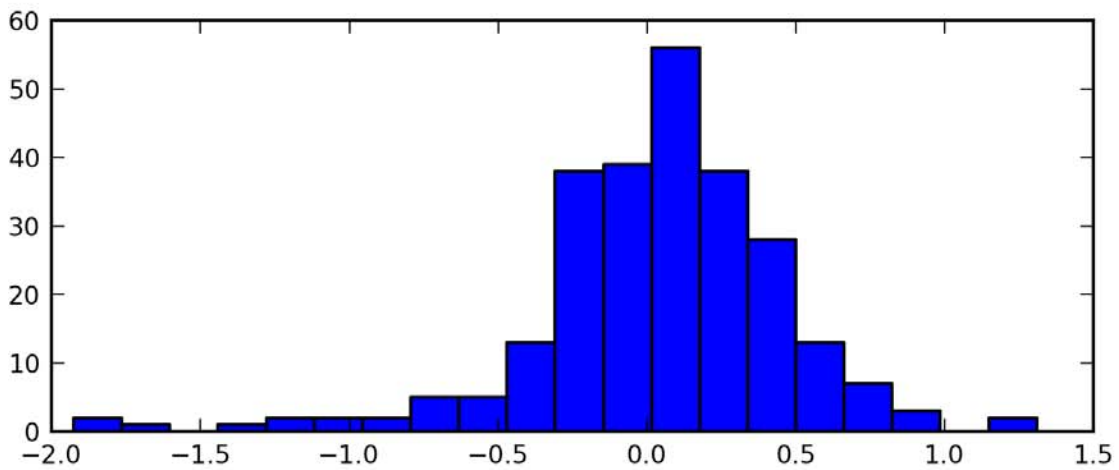

(c) histogram of residuals

Figure 30: Summary of Pareto point 1

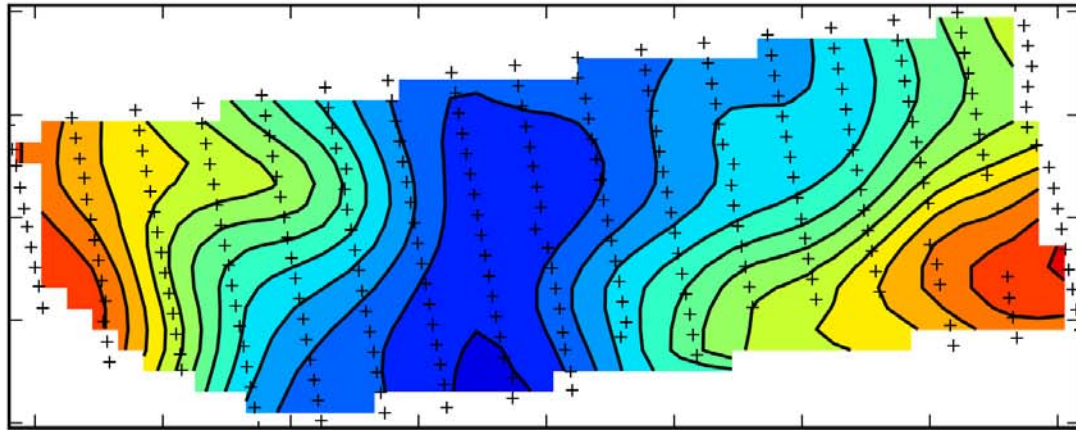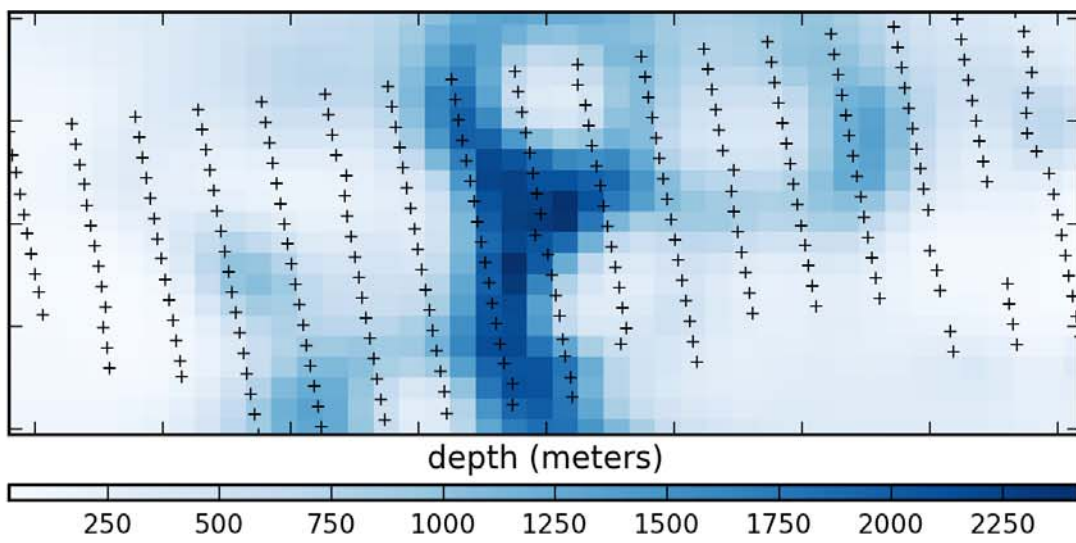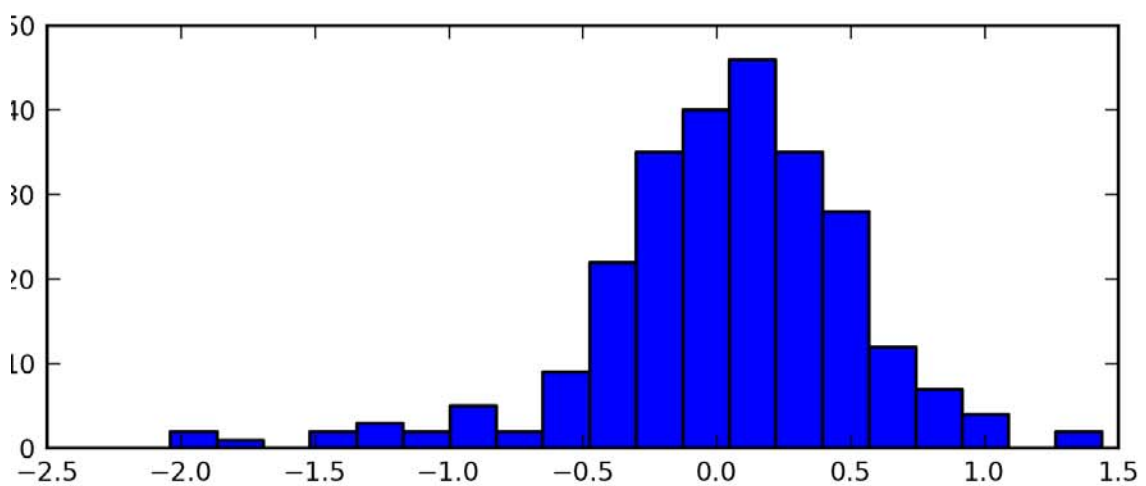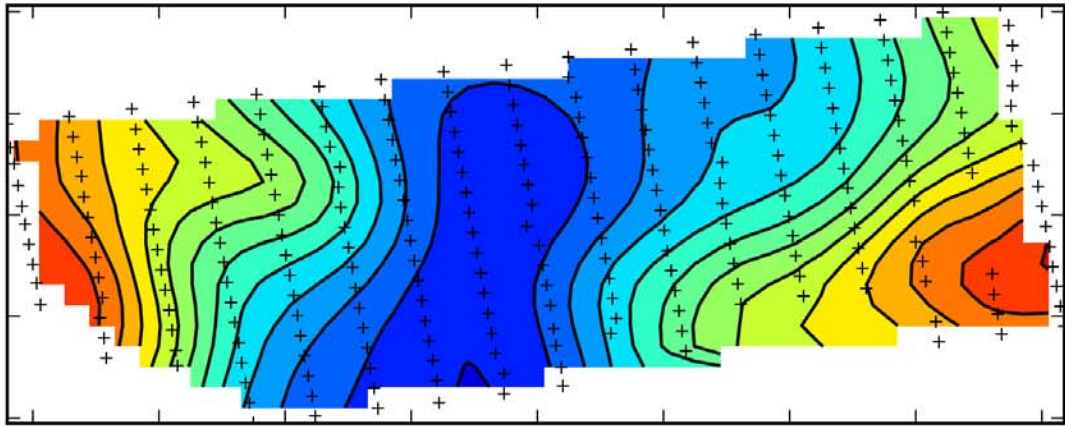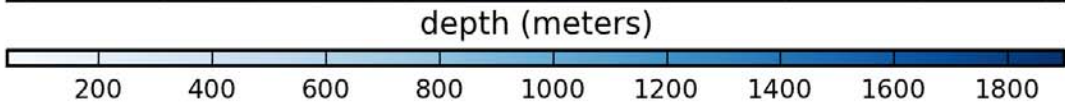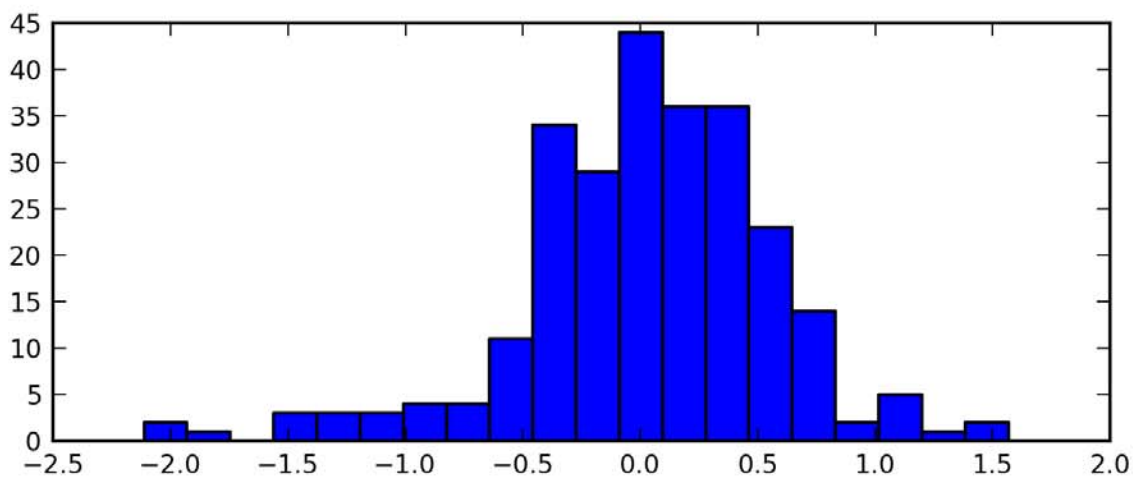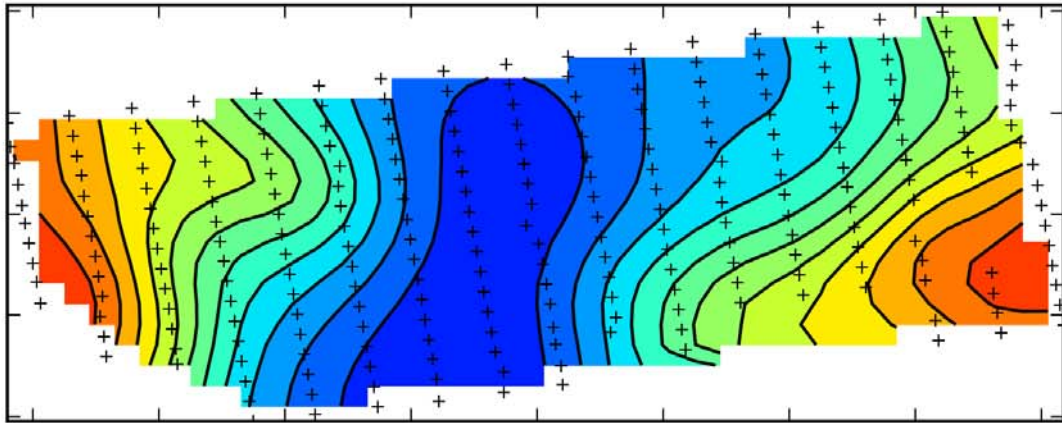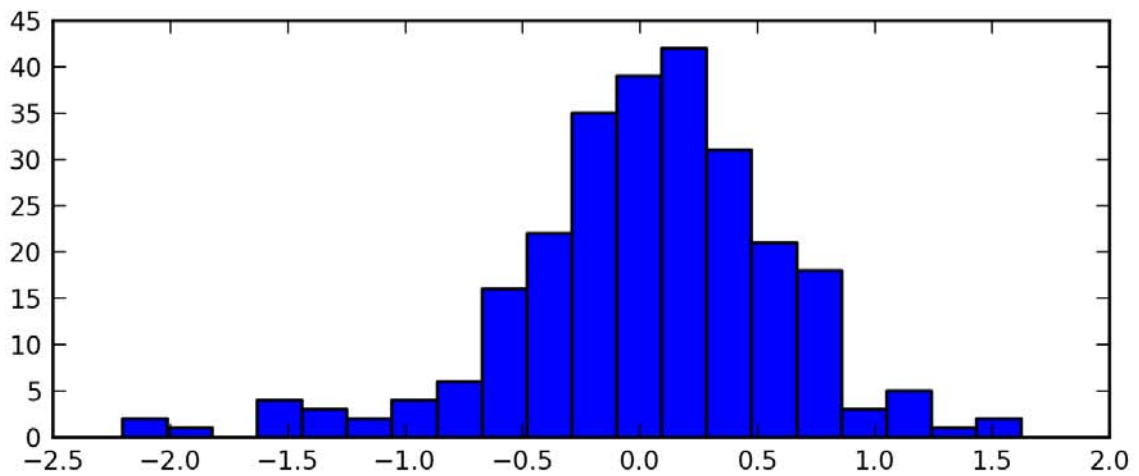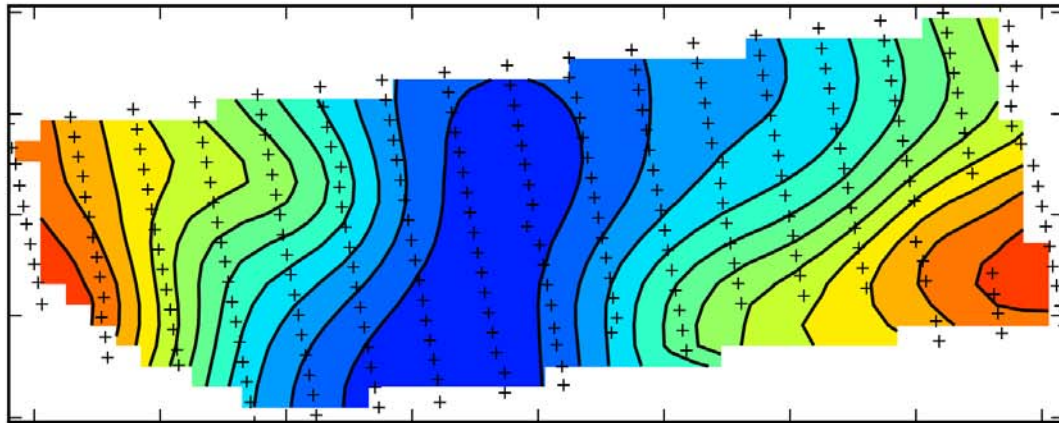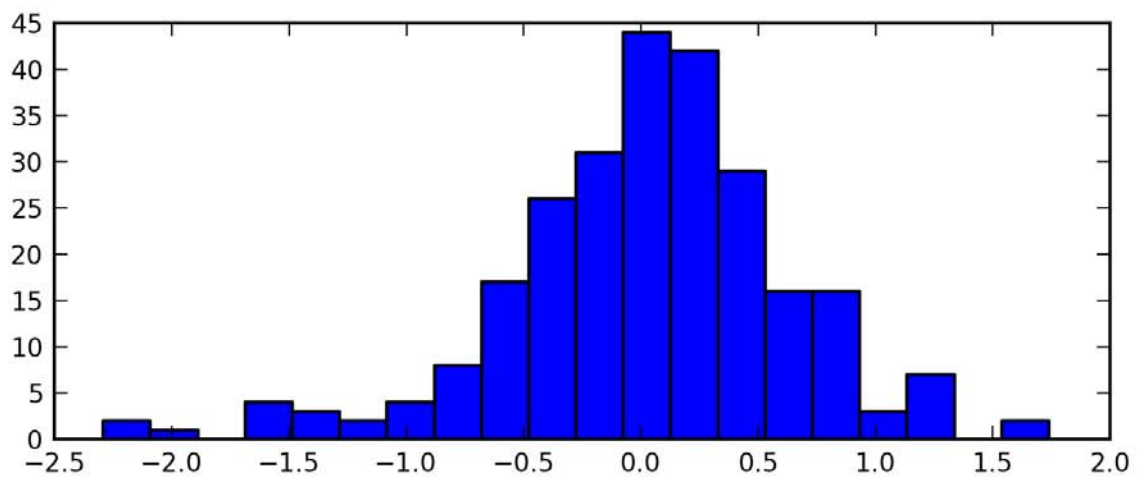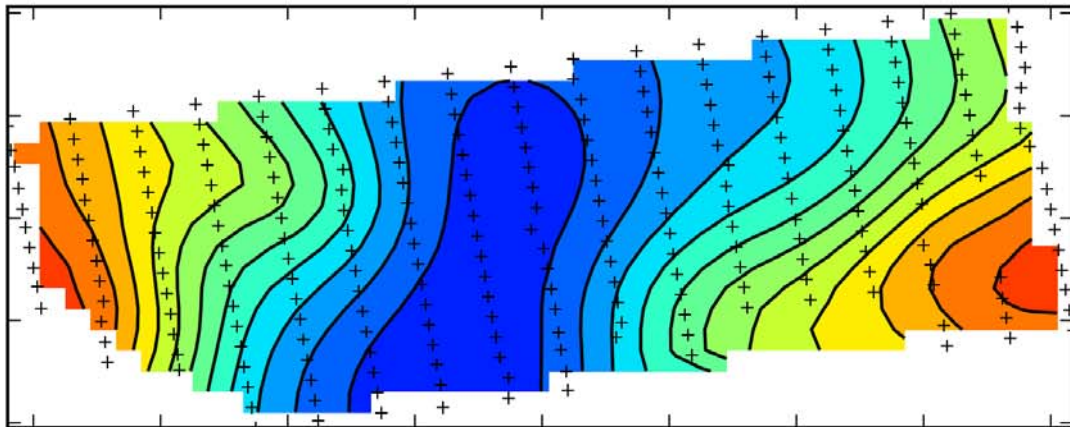(a) simulated gravity response

depth (meters)

(b) inverted depth distribution

(c) histogram of residuals

Figure 31: Summary of Pareto point 2

(a) simulated gravity response

depth (meters)

(b) inverted depth distribution

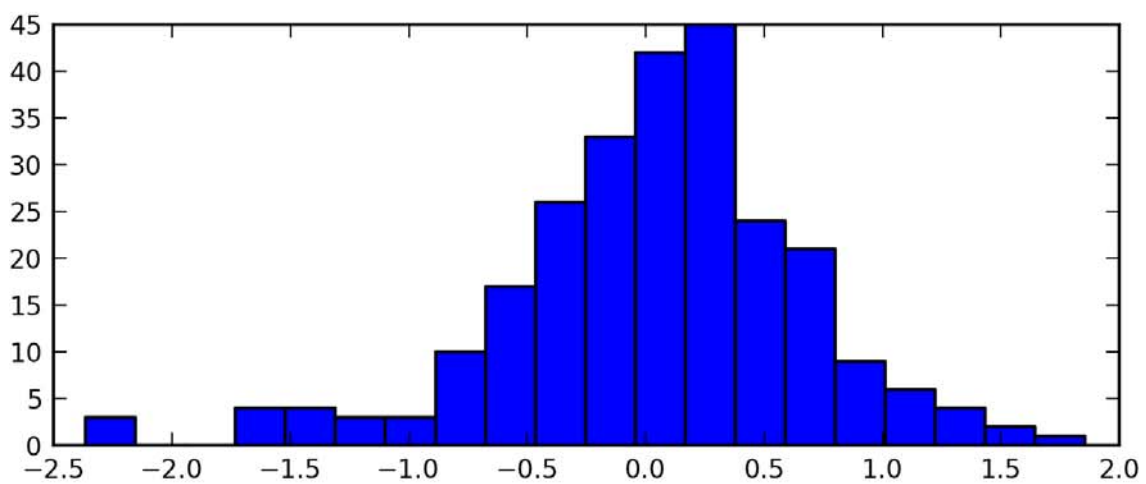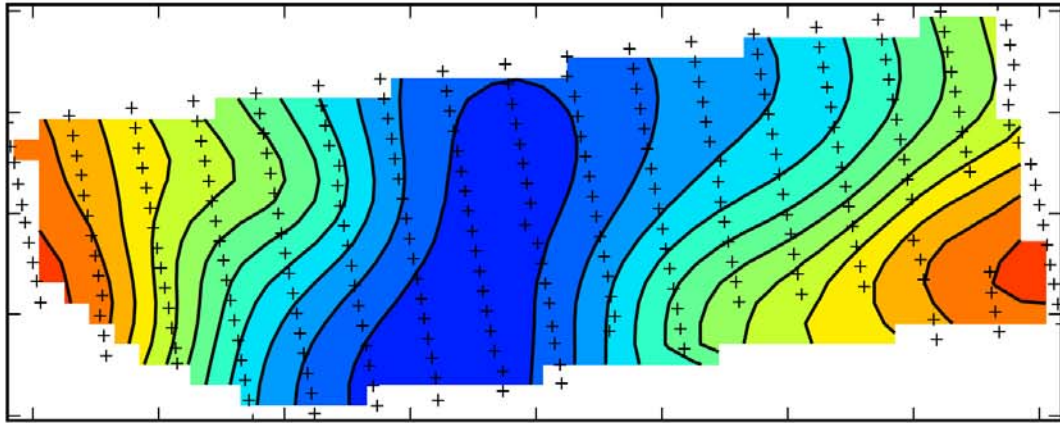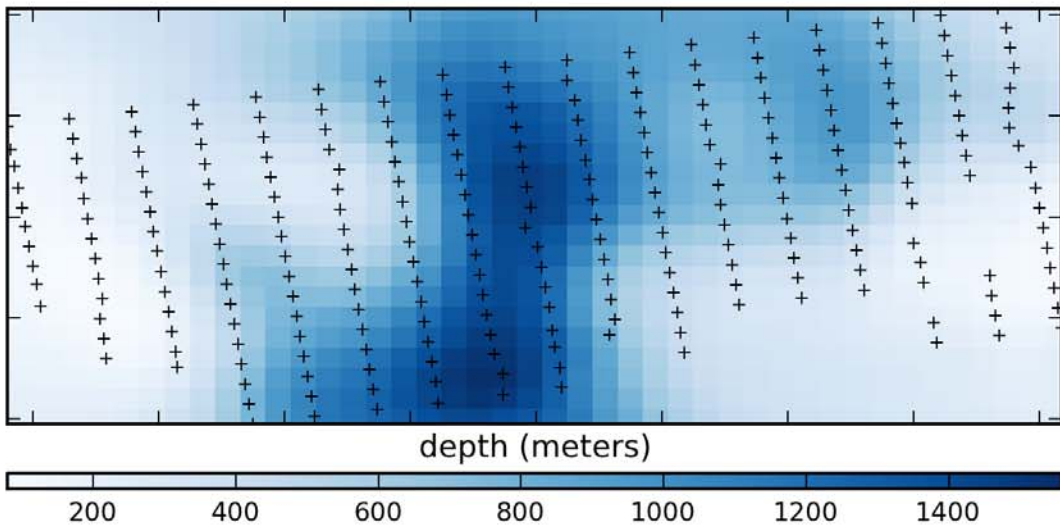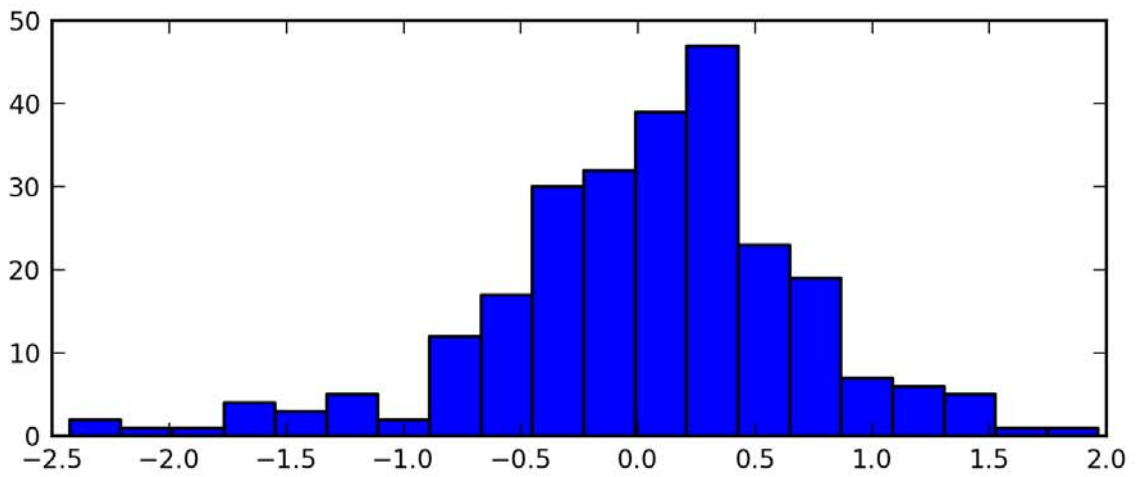(c) histogram of residuals

Figure 32: Summary of Pareto point 3

(a) simulated gravity response
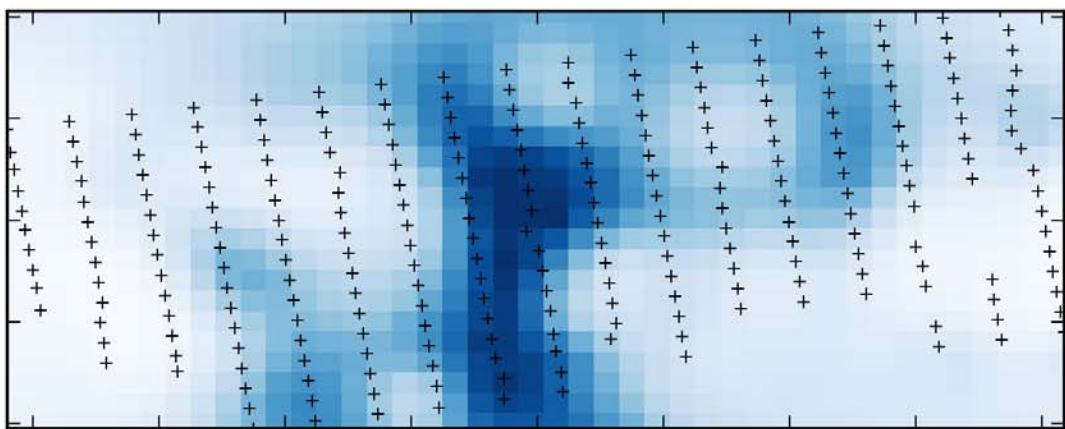
(b) inverted depth distribution

(c) histogram of residuals

Figure 33: Summary of Pareto point 4

(a) simulated gravity response

depth (meters)
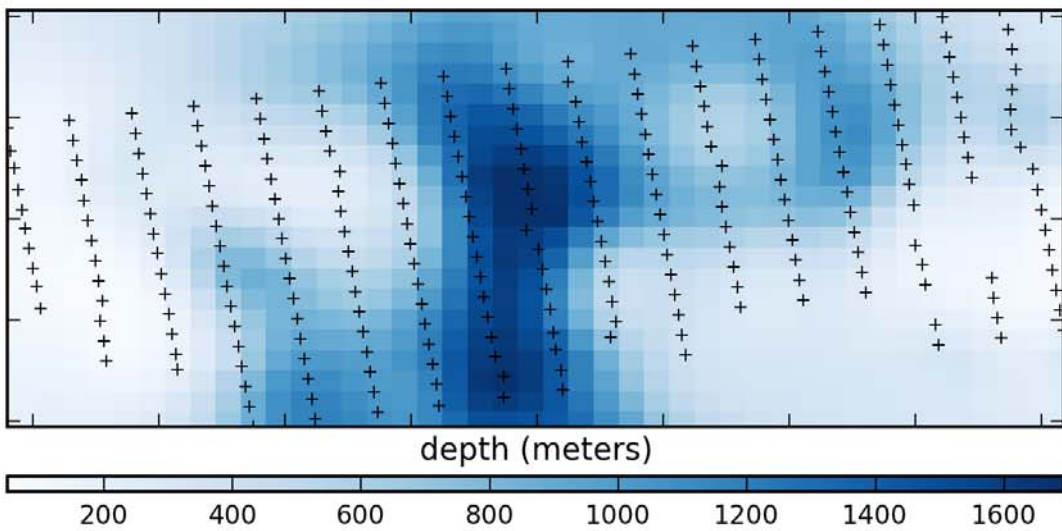
(b) inverted depth distribution

(c) histogram of residuals

Figure 34: Summary of Pareto point 5

(a) simulated gravity response

depth (meters)
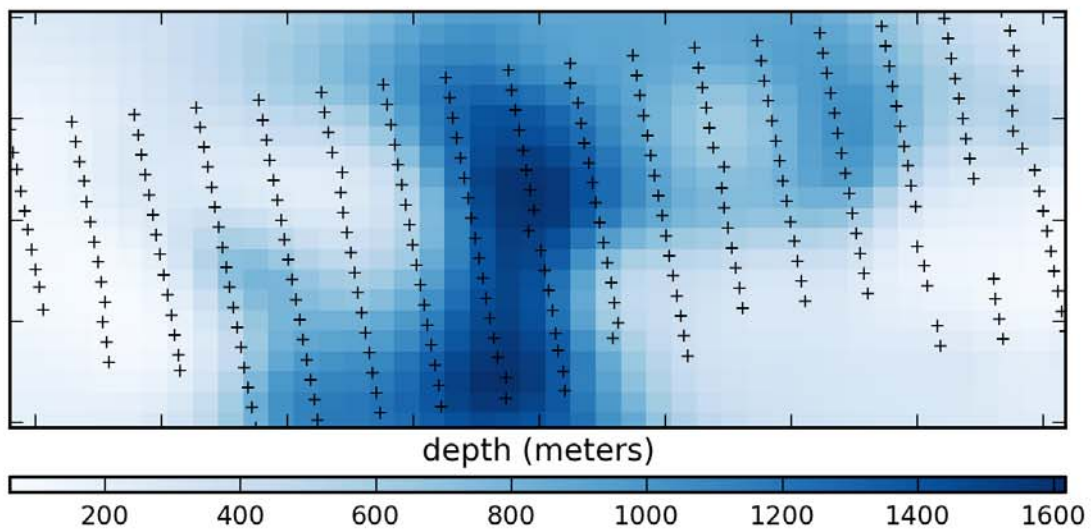
(b) inverted depth distribution

(c) histogram of residuals

Figure 35: Summary of Pareto point 6

(a) simulated gravity response

depth (meters)
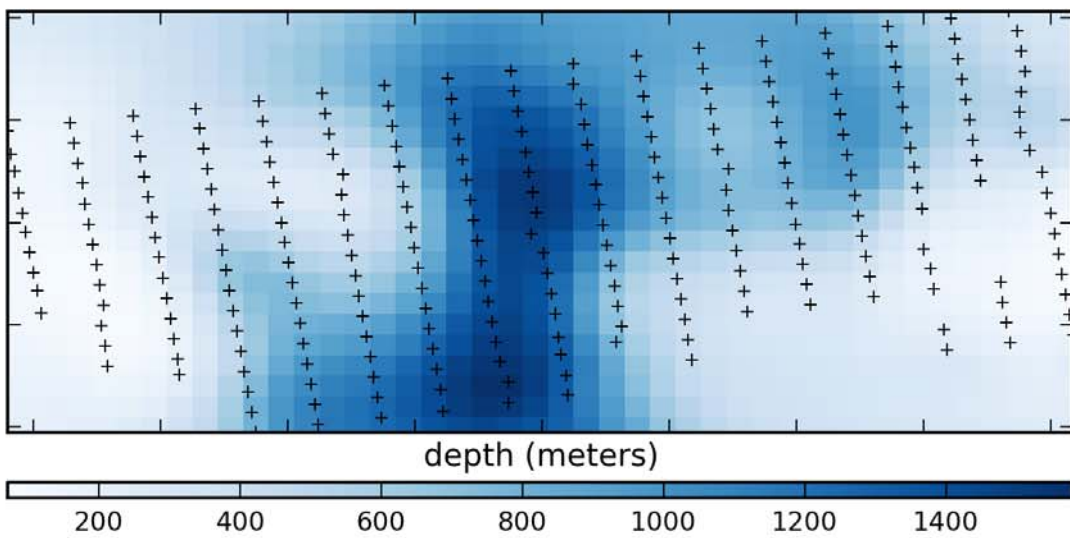
(b) inverted depth distribution

(c) histogram of residuals

Figure 36: Summary of Pareto point 7

37

(a) simulated gravity response

depth (meters)

(b) inverted depth distribution

(c) histogram of residuals

Figure 37: Summary of Pareto point 8
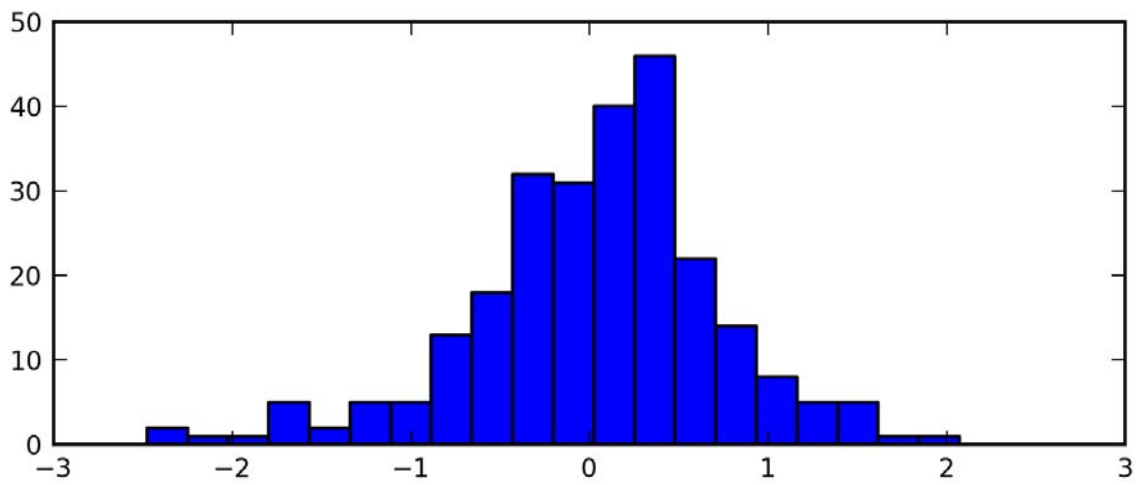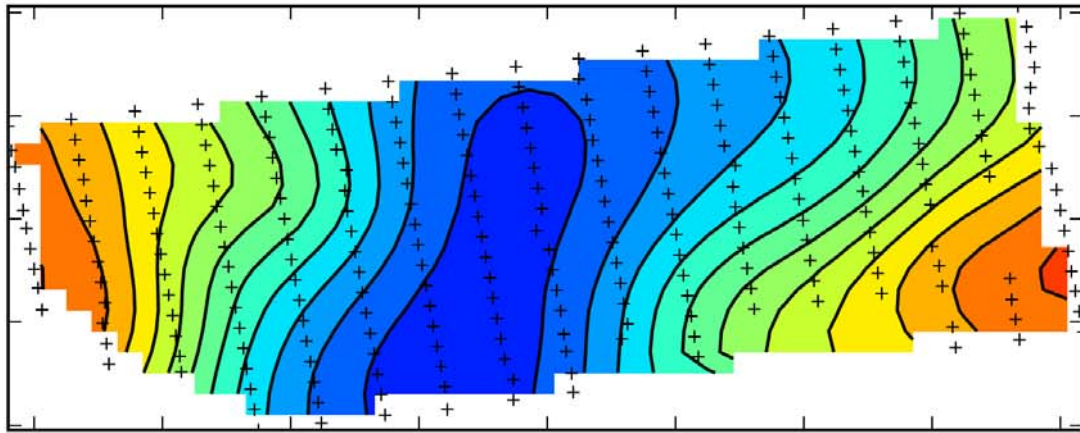
(a) simulated gravity response

depth (meters)

200   400   600   800   1000   1200   1400
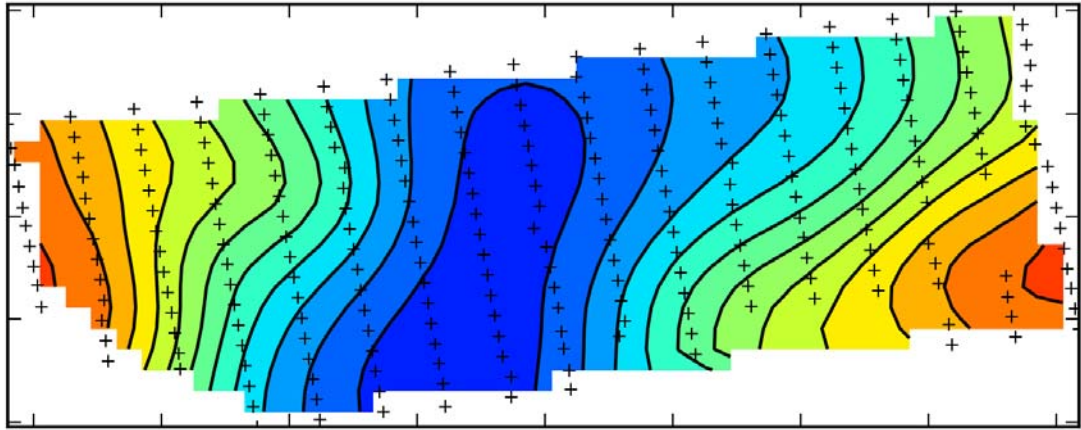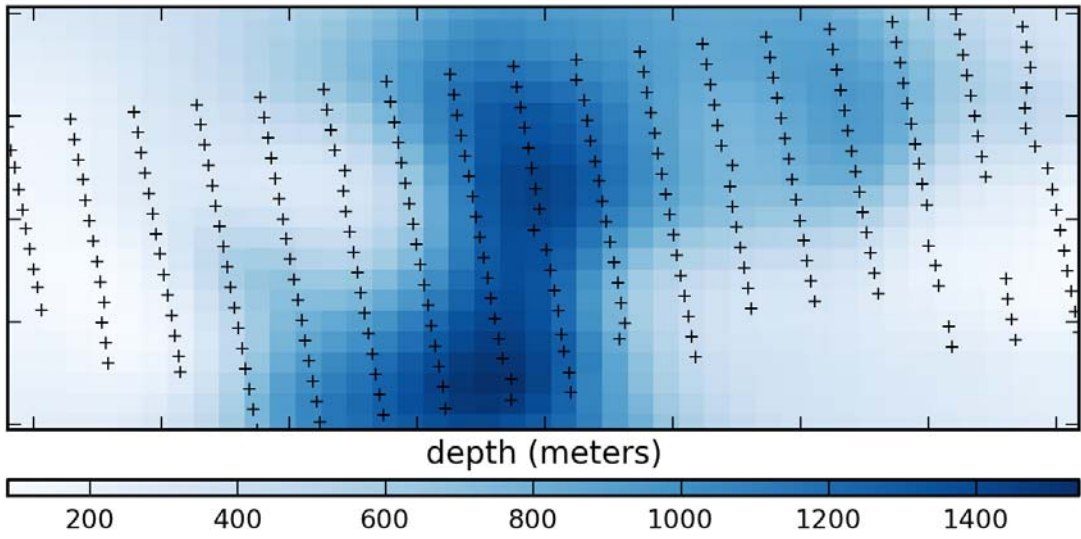
(b) inverted depth distribution

Figure 38: Summary of Pareto point 9
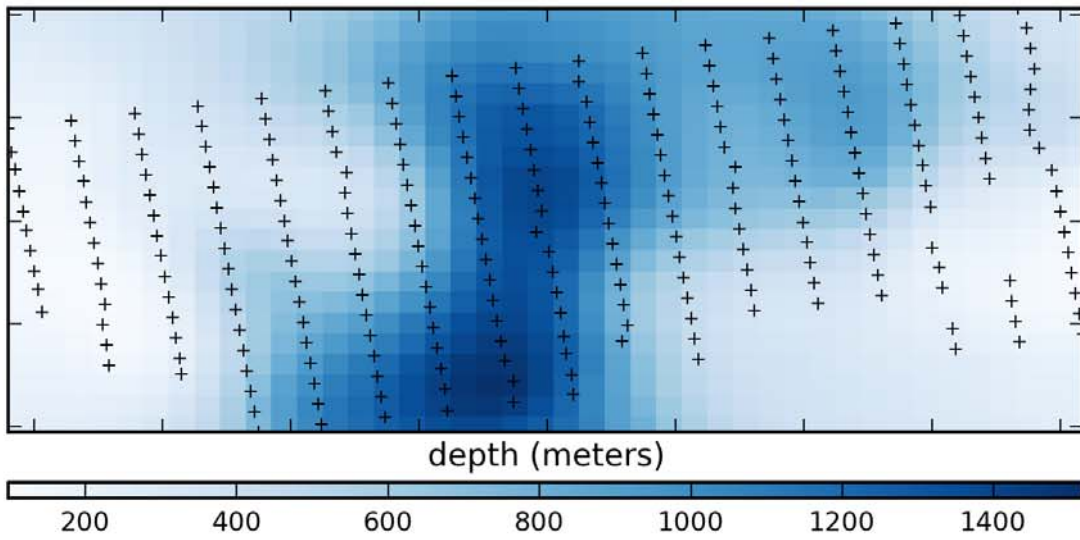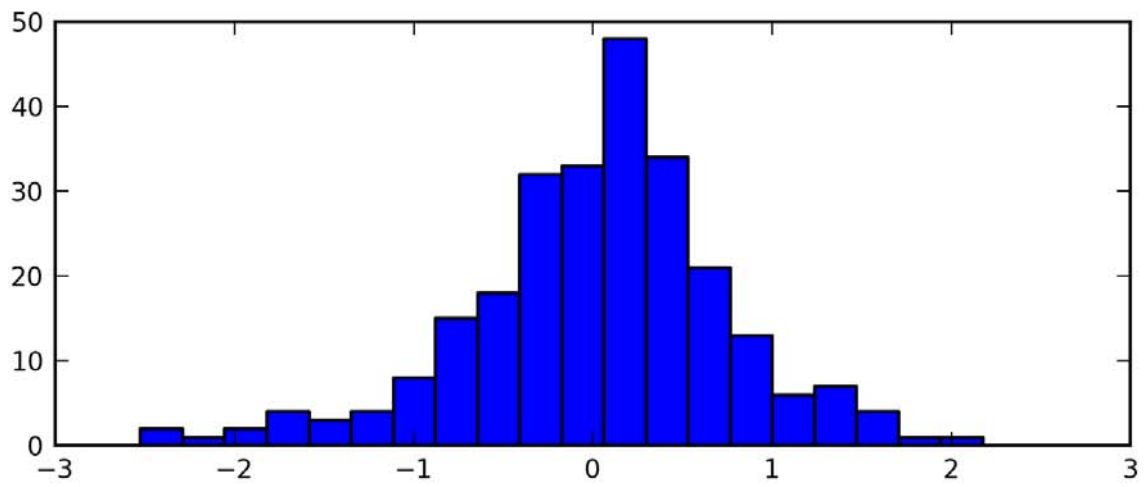
(a) simulated gravity response

depth (meters)

(b) inverted depth distribution

Figure 39: Summary of Pareto point 10